First, we would like to thank the three reviewers for their detailed and constructive comments about this article.

As a main feedback, the three reviewers suggest us to consider more events in our analyses in order to strengthen the quantitative outcomes of this article, especially regarding the PIA-ϕdp relationship in the melting layer (ML). We recognise this is desirable and feasible since we have recorded about 30 events with the ML being at the level of the Moucherotte radar. This will be however a major additional work requiring the collection and processing of the Moucherotte radar data that are not available yet to us, and will not be available in the coming weeks/months due to the covid-19 lockdown.

However, we have extended the rain case study to 9 convective events (new Table 2) and the results obtained nicely confirm the analysis of the first version of the article for the July 21st 2017 convective event.

We have also deepened the methodology and redo all the calculations with a special attention on (i) the characterization of the dry-weather reference targets stability and time variability (new tables 3 and 4, figures modification to show the 10% and 90% quantiles of the apparent reflectivity of the mountain targets) and (ii) on the possible deltahv contamination of the raw psidp profiles. The regularization procedure of the raw phidp profiles was improved in this latter respect and we found it to be efficient in filtering "bumps" likely associated with deltahv contamination.

Regarding the manuscript, the abstract and the conclusion were largely rewritten and the description of the MRT and polarimetry PIA estimators was also much detailed in sections 3.1 and 3.2. Two additional figures were included to better illustrate and support the analyses made.

In general terms, we took great care in discussing the results and the possible influence of the various sources of error in the two different case studies.

We do hope these efforts, which effectively resulted in a major revision, will satisfy the anonymous reviewers.

Our item-by-item replies are inserted below in blue within the reviewers' comments recalled in black.

Anonymous Referee #1

General comment

The manuscript entitled "On the relationship between total differential phase and path integrated attenuation at X-band in an Alpine environment" presents interesting observations of radar measurements conducted at various relative altitudes with respect to the melting layer. The two-radar set-up and the combinations of their measurements is interesting, uncommon, and surely relevant for the radar meteorology community. I believe that the manuscript is suitable for publication after a major review, following the major and minor comments proposed here.

Major comments

1. Let us take as example Figure 4, but this has to be considered as a general comment on how to present the MRT data. When the authors show the reference dry value of reflectivity, I believe they should show also an indication of its variability (standard deviation or quantiles, to put some sort of error bars to the black curve). In my experience, the variability of mountain returns can be significant even at short time scales. This is particularly true as the radar of this manuscript is scanning and not

pointing at a fixed direction. I would be pleased to see a significant section of the manuscript devoted to illustrate and statistically characterize the stability of MRT signals in dry weather before to discuss the analysis and the results of the two cases.

A considerable effort was done in this respect with a detailed description and illustration of the methods used to select the mountain targets and their stability and time variability in the two measurement configurations (new section 3.1). Two tables were added and the figures were modified when needed so as to show the time variability of the mountain targets.

We did not modify Fig.4 however for which the considered mountain returns correspond only to those available for a given radial of the considered target.

2. It would be beneficial if the authors could extend their analysis beyond the focus on two contrasted events only. It would be also more consistent with the title of the manuscript, that suggests a more global approach rather than the analysis of individual precipitation events.

As indicated above we have extended the convective case study to 9 events. We are not in position to do the same work for the ML case study in this period.

We have moderated the ambition of our study by adding "Preliminary investigation of …" in the title of the article

3. While I found the data shown here very interesting, I could not see in the manuscript a clear research goal but rather a showcase of interesting radar observations.

We tried to improve the motivation of this study in several places. Effectively, this study is somewhat "upstream" with respect to the practical goals of the RadAlp experiment which concern rainfall and snowfall estimation in a high-mountain context. This is only one step in a certainly long-term process. The reviewer may recognised the importance of comparing PIAs derived from polarimetry and from direct power estimates and the need to put these 2 estimators in competition for QPE with respect to independent measurements (future step). Attenuation in the ML is also poorly documented and important for the interpretation of radar measurements, especially in our high-mountain context.

Other comments

1. Abstract: I believe that the goals of this research should be better stated in the abstract.

Modification performed:

"We present in this article a methodology for studying the relationship between the differential phase shift due to propagation in precipitation (Φ_{dp}) and path-integrated attenuation (PIA) at X-Band. This relationship is critical for quantitative precipitation estimation (QPE) based on polarimetry due to severe attenuation effects in rain at the considered frequency. In addition, this relationship is still poorly documented in the melting layer (ML) due to the complexity of the hydrometeors' distributions in terms of size, shape and density. The available observation system offers promising features to improve this understanding and to subsequently better process the radar observations in the ML."

2. Page 2, L 53: to my knowledge, the Swiss meteorology office has all the radars installed at high altitude, i.e. it copes with the altitude dilemma by choosing visibility over proximity to the ground. Is it right?

Yes, and this is the same for the French radar network. This is justified for the detection/monitoring of strong and localized convective events at the regional scale that are poorly sensed by conventional

raingauge networks. However, we showed in a previous article that the Moucherotte radar perfoms its measurements within or above the ML in about 70% of cases of significant precipitation in Grenoble, with subsequent increased difficulties for QPE at ground level.

See the following reference:

A.K. KHANAL, G. DELRIEU, F. CAZENAVE and B. BOUDEVILLAIN, 2019. Radar Remote Sensing of Precipitation in High Mountains: Detection and Characterization of Melting Layer in the Grenoble valley, French Alps, *Atmosphere,* 10, 784; doi:10.3390/atmos10120784

3. Page 6, L 173: please consider that in case of hail of cm size, δ can be very large at X-band.

Yes we are aware of this. No hail was reported for the convective cases considered. In addition we took great care in the revision to evidence and try to filter (with some success) the deltahv contaminations, e.g. new Fig.4 left.

4. Page 7, L 200: the clutter identification by means of ρHV should be interpreted as visual, or an algorithm is implemented to discriminate clutter from ρHV ?

See next point

5. Page 7, L 191: was this choice based on comparison with ground-based instruments?

No this choice is based on the ML statistics presented in Khanal et al. (2019)

As detailed in new section 3.2, we flagged as noise all Φ_{dp} gates for which ρ_{hv} < 0.95 for the XPORT rain case study and we determined the beginning and the end of the precipitation range considering a number of successive gates (10, i.e. e range extent of 342 m) for which this threshold was overpassed. Due to the noise affecting rhohv in the ML, we had to considerably lower this threshold (down to 0.8) for the ML case study.

We have abandoned the idea of using a threshold on the reflectivity in the new version of our methodology

6. Page 6-7: is Kdp then simply estimated as gate-by-gate derivative from the clean Φdp, or an estimation method is used?

Yes, the Kdp profile is simply estimated as gate-by-gate derivative of the processed Φ_{dp}profile.

7. Page 11, L 345: would it be possible to show the position of the 16 MRT targets on a map? Also, could it be clarified more in detail how those (gates? pixels?) have been chosen, and which are their statistical properties?

The way the targets are defined is now more detailed in the revision in section 3.1, with 2 additional tables and modification of the relevant figures

8. Section 4.2: this one is in my opinion the most interesting part of the manuscript. I would recommend to expand it, and to apply this methodology to many more precipitation events and aim at results based on a large dataset.

More details have been added to illustrate the methodology and the limitations of this preliminary case study. As explained in the head of the review, we are unfortunately not in position to extend it to other events right now…

9. Figure 4, please show all the polarimetric variables over the same range. For example the Ψdp profile is shorter than the ZH or ρHV profile. If a censoring is applied, please mention it in the caption and describe it in the text.

The Φ_{dp} profile processing / display is voluntarily restricted to the "rainy" region (r0, rM) free of close-range and mountain clutter while the other profiles include the mountain target.

10. Figure 5: please mind the overlapping labels on the y axis.

corrected

Anonymous Referee #2

The manuscript discusses a methodology to investigate the relationship of the radar-derived PIA and the total differential phase in two different interesting precipitation regimes: rain and melting layer. I found the manuscript very well written and understandable and technically correct. That said, I feel that the manuscript lack of significant conclusions. I suggest for major revision.

Main concerns.

1. The main messages to keep home for a reader seems to be i) apply a non-linear fit for k-Kdp relationship in rain to have an more unbiased estimation of PIA and ii) Melting layer attenuation can be estimated using a unique configuration that foresees the use of two radars optimally positioned in a Mountain environment. I find the first finding not very new although useful,

Yes but several publications (e.g. Testud et al. 2000, Schneebeli and Berne 2012) mention the existence of a linear relationship at X-band and the subsequent advantages in terms of QPE. Our preliminary findings seem to indicate that this is not the case and that the rain type may be an important factor controlling this relationship.

whereas I find the second finding interesting although the measurement configuration is far to be generalizable. I think the Authors should add some more text where they discuss their results thinking to a practical-oriented use of their findings. For example, keeping in mind all the limitations recalled by the Authors, do you encourage the use of the parametrization introduced in figure 9 (blue curve) to a have a rough estimation of ML attenuation using a polarimetric radar?

No because in this scatterplot are mixed pairs of estimates obtained from various layers of the melting layer. In the hypothesis of a linear relationship, new Fig. 13 (old Fig 11) is certainly more useful to describe the k-Kdp relationship and its variation within the ML.

2. I was surprised by the fact that having two radars operating at nearly the same frequency in a such interesting configuration, somehow one above and one below the ML, you didn't try to compare the reflectivity factors of the two to have a proxy of the ML attenuation.

This is a good idea that was already explored by our Météo-France co-authors for the other Alpine X-band radars (within the RythMME project). See the following reference:

Yu, N., Gaussiat, N., and Tabary, P.: Polarimetric X-band weather radars for quantitative precipitation estimation in mountainous regions. Q. J. Royal Meteorol. Soc., 144(717), DOI:10.1002/qj.3366, 2018.

Note that an accurate calibration of the two radars is required and that the difference in the resolution volumes limit to some extent the interest of this approach. In addition, our colleague Nan Yu, started looking at the possibility to implement his method to the Grenoble configuration. He

found out that many of the “common measurement gates” of the two radars were actually affected by side-lobe contamination for the MOUC radar.

3. Did you check the radar absolute calibration using DSD Parsivel data?

The MOUC radar calibration was performed through the Météo-France standard electronic calibration procedure followed by a qualification of the rain products through radar-raingauge comparisons. The XPORT radar electronic calibration was performed at various occasions during the radar implementation in several campaigns. No radar-raingauge or radar-disdrometer comparisons have been made so far in the Grenoble context. In any case, a major advantage of the proposed methodology is that both the Φ_{dp} and the MRT PIA estimates are independent of eventual radar calibration errors.

4. MRT variability is never discussed in this manuscript. Do you think it can explain part of the variability in figure 8, y-axis?

As requested by reviewer #1, we have added a lot of material in the revision regarding the mountain return stability and time variability. For the rain case, we believe this factor to be of very limited importance due to the very small variability of the mountain returns. More impact is likely for the ML case but we don’t think this is a dominant source of error.

Anonymous Referee #3

1 Summary

This manuscript proposes a data-driven investigation of the relationship between the differential phase shift and the specific attenuation in rain, melting snow and snow, using an original instrumental set-up consisting of two X-band polarimetric radars at different altitudes in the complex terrain around an Alpine valley. Such relationships are crucial to accurately correct for attenuation in precipitation to obtain reliable quantitative precipitation estimates at X-band. The path integrated attenuation is determined using strong (fixed) mountains echoes at various distances from the considered radar

from the two considered radars…

and provide independent estimates that can be compared to the (total) differential phase shift derived from polarimetric radar measurements. In rain, additional information about the raindrop size distribution measured by a disdrometer at the ground level is available to compute theoretical relationships. Focusing on two contrasted event (one convective and the other with a transition from snow to rain), the authors quantify the respective values of PIA and total differential phase shift from a number of mountains echoes, in rain using the lower radar, and in snow and in the melting layer using the higher radar. In this way, the specific attenuation in the ML can be quantified and it appears that the relationship between the PIA and the total differential phase shift is not that linear.

To be more precise, in the ML (stratiform case), old Fig. 11 suggests that the multiplicative coefficient of a k-Kdp relationship (assumed to be linear) depends on the position within the ML and as such on the melting processes.

2 Recommendation

The manuscript is clear, the methods are sound and properly described. Such characterization of the attenuation in the melting layer and its links with the differential phase shift are relevant to the

weather radar community and to AMT readership. I have some concerns and suggestions listed below, I hence recommend to send the manuscript back to the authors for major revisions.

3 General comments

1. The main concern in my view is the limited amount of data analyzed. The representativity of these two events, and the one used to investigate attenuation and differential phase shift in the melting layer is not clearly addressed: to what extent can a reader use the numbers provided here for other locations/seasons? This is an important aspect because if not representative, the obtained results will be of limited interest to potential readers (who may not be able to reproduce the same instrumental set-up involving two radars and complex terrain). The authors touch upon this issue in the conclusions and mention that they will process more data, but this should be addressed earlier in the text, and to be honest I am wondering if they should not do so already in this manuscript.

We fully understand this comment but we are not in position to extend our analyses to other ML cases right now, see our head comment… We have extended the convective case study to 9 events.

2. The scientific objectives of the manuscript are not very clear. What are the main take-home messages for the reader?

We have tried to improve this aspect in the conclusion of the article (and in the abstract).

Message 1 about the rain case study in the conclusion:

"In the end, the scatterplot of the MRT PIAs as a function of the $\phi_{dp}(r_M)$ for all the nine convective events presents an overall good coherence with however a significant dispersion (explained variance of 77%). It is interesting to note that the non-linear $k - K_{dp}$ relationship derived from independent DSD measurements taken during the events of interest at ground level allows a satisfactory transformation of the XPORT ϕ_{dp} profiles into almost unbiased (although dispersed) PIA estimates. Both estimation methods are prone to specific errors and, even if the MRT PIA estimator is more directly related to power attenuation, it is *a priori* difficult to say which estimator is the best. An assessment exercise of attenuation correction algorithms, making use of both PIA estimators, with respect to an independent data source (e.g. raingauge measurements) is desirable to distinguish the two PIA estimators. A specific experiment is being designed in this perspective to be implemented in the near future."

Message 2 about the ML case study:

"From this dataset, it was possible to derive the evolution of $PIA(r_M)$ and $\phi_{dp}(r_M)$ values as a function of the altitude within the ML. The evolution with the altitude of the ratio of the mean value of $PIA(r_M)$ over the mean value of $\phi_{dp}(r_M)$, as a proxy for the slope of a linear $k - K_{dp}$ relationship within the ML, was also considered… The three variables considered present a clear signature as a function of the (scaled) altitude. In particular, the PIA/ϕ_{dp} ratio peaks at the level of the ρ_{hv} peak (somewhat lower than the Zh peak), with a value of 0.42 dB degree^{-1}, while its value in rain just below the ML is 0.33 dB degree^{-1}. … Although the experimental configuration for the study of attenuation in the ML presents some limitations (radome attenuation, NUBF), the preliminary results presented here will be deepened by processing a dataset of about thirty stratiform events with the presence of the ML at the level of the MOUC radar.

3. The assumption that the differential phase shift on backscatter (δhv) is negligible is not really justified.

This comment led us to a big consideration of this point during the revision process. Besides the cited literature we have searched evidence of deltahv contamination in the raw psidp profiles both for the convective cases and the stratifom one. We have found some “bumpy” profiles during some convective events that our regularization procedure is fortunately able to filter in a nice way. No bumpy profiles in the stratiform case. But we recognise that more work is required on this topic…

Together with the possible PIA overestimation due to radome attenuation for the MOUC radar during the stratiform event, these two sources of uncertainties may affect the highlighted behavior of the ratio between the PIA and the Ψdp in the ML. This aspect should be clarified.

This is actually hard to clarify.

In addition to the delthv contamination, the radome attenuation is a real concern. We have considered a mountain target in the vicinity of the MOUC radar (5 km or so) but it was too unstable to provide useful information. We have tried to be more careful in our interpretations of this very limited case study ; see our new comments of the results obtained on the upper part of the ML (which could sign radome attenuation or NUBF effects). Radome attenuation is likely small for the considered case due to the low rainrates/snowrates and the fact the radome is heated.

4 Specific comments

1. Title: I think the exact term is differential phase shift. I recommend the authors to edit the whole text to add shift where needed.

OK, done

2. P.1, l.12: rainfall and snowfall rather than rain and snow.

corrected

3. P.1, l.13: “high mountain regions": the adjective high is relative... I suggest to change to “mountainous regions".

Although relative, we want to keep the adjective “high” since radar QPE is particularly challenging in such regions wrt to plains or medium-elevation mountains

4. P.1, l.24: high rather than strong rain rates.

corrected

5. P.1, l.24: Φdp is not defined yet.

corrected

6. P.2, l.41: insert “over extended areas" between “achieved" and “with traditional".

done

7. P.2, l.42-51: it would be good to support the statements by references to the literature.

These statements are quite “generic” and do not require in our view specific referencing.

8. P.2, l.58: the common usage is that polarimetric means dual-polarization and Doppler...

Good point, we suppressed “Doppler”

9. P.3, l.72: Kdp is the specific differential phase shift on propagation. Please correct wherever needed in the text.

corrected

10. P.4, Section 2.1: what about the calibration of the two radars? How was it checked/performed?

The MOUC radar calibration was performed through the Météo-France standard electronic calibration procedure followed by a qualification of the rain products through radar-raingauge comparisons. The XPORT radar electronic calibration was performed at various occasions during the radar implementation in several campaigns. No radar-raingauge or radar-disdrometer comparisons have been made so far in the Grenoble context. In any case, a major advantage of the proposed methodology is that both the Φ_{dp} and the MRT PIA estimates are independent of eventual radar calibration errors.

11. P.4, l.110: missing closing bracket after “study".

corrected

12. P.5, Eq.1: This equation is for a given polarization, this should be indicated using a subscript h/v for instance.

The following sentence was added:

Note that PIAs can be obtained from eq.1 for both the horizontal and the vertical polarizations. In the present article, we will restrict ourselves to the horizontal polarization, the study of differential attenuation being a possible topic for a future study.

13. P.6, l.168: δhv is the differential phase shift on backscatter.

OK corrected

14. P.6, l.175: the units of these ranges of values (degree?) should be provided.

done

15. P.6, l.179: the assumption of negligible δhv should be better justified. A few degrees for δhv as suggested on l.175 are not necessarily negligible compared to the overall Ψdp values provided in Fig.10 for instance. As mentioned in the General Comments, the resulting uncertainty in Φdp values may affect the behavior highlighted in Fig.10 and 11. Combined with possible radome attenuation...

Yes we agree, but there is little possibility to go further… We have expended and moderated our comments of new Figs 12 and 13 in section 4.2 and in the conclusion.

16. P.6, l.182-183: why N = 10 and N = 4? How did you come up with these values?

This is empirical.

17. P.7, l.191: same here, please justify these thresholds in Zh and ρhv.

Actually for the Φ_{dp} profile processing for the convective case (without ML interaction), we determine now the beginning and the end in range of rain cells undisturbed by clutter by using a rhohv threshold only ($\rho_{hv} \geq 0.95$) to be valid over a number of successive gates (10 gates for XPORT radar, i.e. a range extent of 342 m). We had to adapt these figures for the MOUC radar due to the well-known decrease of rhohv in the ML ($\rho_{hv} \geq 0.80$, and 2 successive gates, that is 480 m) and to consider the actual range of the first mountain gate for the determination of rM.

18. P.7, l.196: the black line in Fig.4 represents the instantaneous values of Zh, it would benice to figure the variability of the mountain return, to give the reader an idea about the noise of such echoes (and hence an idea about the uncertainty in the derived PIA estimates).

We have added a lot of material in the revision about the stability and time variability of the dry-weather mountain returns of the various targtes. We did not modify Fig.4 however for which the considered mountain returns correspond only to those available for a given radial of the considered target.

19. P.8, l.218: please provide a reference for negligible attenuation in snow.

done

20. P.8, l.228: “[7]" seems to be a literature reference, but there is no number in the references. Please update.

corrected

21. P.8, l.245: the co-fluctuation between the two signals does not look that bad by eye... Maybe you could compute the correlation coefficient to have a quantitative criterion?

The number of pairs of points is quite low for individual targets. The results for the ensemble of targets is displayed in new Fig.11 (old Fig 9).

22. P.8, l.242-248: the possible influence of beam broadening and radome attenuation (see l.401-406) could be first mentioned here.

Yes, we have added a paragraph on the possible error sources at the end of section 3.2

23. P.9, l.277: change citations from numbers ([10] and [19]) to author’s names...

done

24. P.10, l.302 and Fig.8: I may be wrong, but I think there is an issue with the axis labels in Fig.8: PIA from polarimetry should be on the y axis while the PIA from MRT should be on the x-axis. Otherwise, there would be an underestimation from the polarimetric approach (slope > 1), not consistent with Fig.6 left. Please clarify.

Very good point! But I confirm that the MRT PIA is on the y-axis and the polarimetry-derived PIA is on the x-axis. As explained in the revised manuscript, this effect is related to the different ranges of Kdp values considered in the DSD analyses and in the Kdp range profiles discretized at 34.2 m. We have checked the stability of the non-linear relation when considering 1-min DSD samples, leading to an extended Kdp range.

25. P.11, l.322-323: what can explain this variability in the ML depth? If this is due to different types of hydrometeors, is the scaling approach used here still relevant?

We think this variability of the ML thickness (with high values between 2:30 and 3:00 UTC, visible on the bottom graph of Fig. 5) to be due to the arrival of the hotter air mass and some kind of atmospheric mixing. We preferred this altitude scaling to the display of absolute altitudes with respect to e.g. the reflectivity or the rhohv peak altitude since the ML thickness varies significantly and the curves of the various ML characteristic points (peaks and inflexion points of Zh and rhohv) evolve rather harmoniously during the ML rise.

26. P.11, l.342: could this less evident shift between peak in Zh and in ρhv be also due to beam broadening? As the ML is going up in altitude, it is also going further away in the PPI used to extract the polarimetric radar variables...

Maybe… However, in the more systematic study of the ML described in Khanal et al. 2019, the shift between the two peaks has been evidenced for MLs at the altitude range of the last part of the January 4th 2018 event. We don't think this point alters the conclusions made in this article.

27. P.12, l.379: why are δhv values expressed in dB?

It was a mistake, corrected, thanks!

28. P.13, l.405-406: but the attenuation due to wet snow sticking on the radome is not necessarily directly proportional to the rain rate (it can accumulates...). The assumption of negligible radome attenuation during the ML scans should be better justified. As it could have significant impact on the estimated PIA values and hence on the behavior of the ratio PIA/Ψdp in Fig.11.

We have to mention that the radome of the MOUC radar is heated, so that snow may not accumulate that much over it. In addition snow/rain rates were low, so radome attenuation may be low in this case. But it is difficult to be sure, and this is certainly a major limitation of our current measurement configuration...

29. P.17, Table 1: the spectral width is not recorded?

Yes for the MOUC radar, no for the XPORT radar at that time; but we didn't use Doppler data in this study

30. P.19, Fig.2: it would be better to use the same y axis scale between the 2 events, to ease the comparison.

Not done! The required code was not available to the main author at the time of the revision (lockdown…)

31. P.20, Fig.3: the underlying images are too coarse in resolution. They should be improved.

done

32. P.21, Fig.4: As expected, the phase measurements are contaminated by clutter earlier (i.e. closer to the radar) than reflectivity measurements. Hence the last (starting from the radar) reliable gate in Ψdp may be closer to the radar than the last reliable gate in Zh from which the PIA is estimated. Could this introduce a bias?

The Φ_{dp} processing (and the subsequent polarimetry-derived PIA estimation) is made on the range of gates non contaminated by close-range or mountain clutter. The MRT PIA includes "on-site" attenuation and attenuation "over" the mountain. So yes, this could introduce a bias, which is difficult to estimate, but that we think of limited magnitude in the considered examples. This is mentioned in the revision.

~~On~~Preliminary investigation of the relationship between ~~total~~ differential phase shift and path-integrated attenuation at X-band in an Alpine environment

Guy Delrieu[1], Anil Kumar Khanal[1], Nan Yu[2], Frédéric Cazenave[1], Brice Boudevillain[1], and Nicolas Gaussiat[2]

1 Institute for Geosciences and Environmental research (IGE), UMR 5001 (Université Grenoble Alpes, CNRS, IRD~~, Grenoble-INP~~), Grenoble, France

2 Centre de Météorologie Radar, Direction des Systèmes d'Observation, Météo France, Toulouse, France

Correspondence to: guy.delrieu@univ-grenoble-alpes.fr

Abstract. The RadAlp experiment aims at developing advanced methods for ~~rain~~rainfall and ~~snow~~snowfall estimation using weather radar remote sensing techniques in high mountain regions for improved water resource assessment and hydrological risk mitigation. A unique observation system has been deployed since 2016 in the Grenoble region, France. It is composed of ~~a~~an X-band radar operated by Météo-France on top of the Mt Moucherotte (~~1970~~1901 m asl; MOUC radar hereinafter). In the Grenoble valley (220 m asl), we operate a research X-band radar called XPORT and *in situ* sensors (weather station, rain gauge, disdrometer). We present in this article a methodology for studying the relationship between the ~~total~~ differential phase (~~ψ_{dp}~~shift due to propagation in precipitation (Φ_{dp}) and path-integrated attenuation (PIA) at X-Band~~, a~~. This relationship is critical for ~~the implementation of attenuation corrections~~quantitative precipitation estimation (QPE) based on polarimetry due to severe attenuation effects in rain at the considered frequency. Furthermore, this relationship is still poorly documented in the melting layer (ML) due to the complexity of the hydrometeors' distributions in terms of size, shape and density. The available observation system offers promising features to improve this understanding and to subsequently better process the radar observations in the ML. We use the Mountain Reference Technique for direct PIA estimations associated with the decrease of returns from mountain targets during precipitation events. The polarimetric PIA estimations are based on the regularization of the ~~ψ_{dp} radial~~ profiles ~~and their derivation in terms~~ of ~~specific~~the total differential phase shift (Ψ_{dp}) from which the specific differential phase shift on propagation (K_{dp}) profiles~~,~~ are derived. This is followed by the application of relationships between the specific attenuation (k) and the specific differential phase shift. Such $k - K_{dp}$ relationships are estimated for rain by using available drop size distribution (DSD) measurements~~, empirical oblateness models for raindrops and a scattering model.~~ available at ground level. Two ~~contrasted~~sets of precipitation events are considered in this preliminary study: (i) ~~a~~nine convective ~~case~~cases with ~~strong rainrates~~high rain rates which allows us to study the $\phi_{dp} - PIA$ relationship in rain; (ii)~~during~~ a stratiform case with moderate rainrates, for which the melting layer (ML) rose up from about 1000 m asl

up to 2500 m asl, where we were able to perform a horizontal scanning of the ML with the MOUC radar and a detailed analysis of the $\phi_{dp} - PIA$ relationship in the various ~~parts of the ML. The~~layers of the ML. A common methodology was developed for the two configurations with some specific parameterizations. The various sources of error affecting the two PIA estimators are discussed: stability of the dry-weather mountain reference targets, radome attenuation, noise of the total differential phase shift profiles, contamination due to the differential phase shift on backscatter, relevance of the $k - K_{dp}$ relationship derived from DSD measurements, etc. In the end, the rain case study indicates that the relationship between MRT-derived PIAs and polarimetry-derived PIAs presents an overall coherence but quite a considerable dispersion (explained variance of 0.~~72) in rain.~~77). Interestingly, the non-linear $k - K_{dp}$ relationship derived from independent DSD measurements ~~allows obtaining~~yields almost unbiased PIA estimates. For the stratiform case, clear signatures of the MRT-derived PIA, the corresponding ϕ_{dp} value and their ratio are evidenced within the ML. In particular, the averaged PIA/ψ_{dp} ~~ratio~~ ϕ_{dp} ratio, a proxy for the slope of a linear $k - K_{dp}$ relationship in the ML, peaks ~~within the melting layer~~ at the level of the co-polar correlation coefficient (ρ_{hv}) peak, just below the reflectivity peak, with a value of about 0.~~4~~42 dB degree^{-1}. Its value in rain below the ML is 0.~~27~~33 dB degree^{-1}, in ~~very~~rather good agreement with the slope of the linear $k - K_{dp}$ relationship derived from DSD measurements at ground level. The $PIA/\psi_{dp}\phi_{dp}$ ratio remains quite ~~strong~~high in the upper part of the ML, between 0.32 and 0.38 dB degree^{-1}, before tending towards 0 above the ML.

1 Introduction

Estimation of atmospheric precipitation (solid / liquid) is ~~of paramount importance~~important in a ~~mountainous~~high mountain region such as the Alps for the assessment and management of water and snow resources for drinking water, hydro-power production, agriculture and tourism, characterized by high seasonal variability. One of the most critical application concerns the prediction of natural hazards associated with intense precipitation and melting of snowpacks, i.e. inundations, floods, flash floods and gravitational movements, which requires a high-resolution observation: spatial resolution $\leq 1km^2$ and temporal resolution $\leq 1hr$. While this can hardly be achieved over extended areas with traditional *in-situ* raingauge networks, the use of radar remote sensing has a high potential that needs to be exploited but also a number of limitations that need to be ~~overpassed~~surpassed. Quantitative Precipitation Estimation (QPE) with radar remote sensing in a complex terrain such as the Alps is made challenging by the topography and the space-time structure and dynamics of precipitation systems. Radar coverage of the mountain regions brings the following dilemma. On the one hand, installing a radar at the top of a mountain allows a 360° panoramic view and therefore the ability to detect precipitation systems over a long range at the regional scale. This is particularly relevant for localized and heavy convective systems in warm seasons. But the precipitation is likely to undergo significant change in between detection and arrival at ground level, including a phase change when the 0° C isotherm is located at the level of or lower than the radar ~~elevation.~~beam altitude. Such situations are likely to be frequent during cold periods, with a strong impact on QPE quality at ground level. On the other hand, installing a radar at the bottom of the valley

provides high resolution and quality data required for vulnerable and densely populated Alpine valleys, but the QPEs are limited at the latter due to beam blockage by surrounding mountains.

MeteoSwiss has a long-standing experience in operating its C-band radar network in the Alps (Joss and Lee, 1995; Germann et al. 2006) and at coping with the associated altitude dilemma. In addition to physically-based radar data processing aimed at determining vertical profiles of reflectivity and at taking benefit of polarimetry, sophisticated radar-raingauge merging techniques and echo tracking techniques, as well as numerical prediction models outputs (Sideris et al. 2014; Foresti et al. 2018) are implemented to better understand and quantify the complexity of precipitation distribution in such a rugged environment. More recently, Météo-France has chosen to complement the coverage of its operational radar network ARAMIS (for Application Radar à la Météorologie Infra-Synoptique) in the Alps by means of X-Band polarimetric ~~and Doppler~~ radars. A first set of three radars was installed in Southern Alps within the RHyTMME project (Risques Hydrométéorologiques en Territoires de Montagnes et Méditerranéens) in the period 2008-2013 at Montagne de Maurel (1770 m above sea level, asl), Mont Colombis (1740 m asl) and Vars Mayt (2400 m asl) (Westrelin et al. 2012). This effort has been continued in 2014-2015 with the installation of an additional X-band radar system (MOUC radar, hereinafter) on top of the Mount Moucherotte (1920 m) that dominates the valley of Grenoble, the biggest city in the French Alps with about 500,000 inhabitants. The choice of the X-Band frequency is challenging due to its sensitivity to attenuation (e.g. Delrieu et al. 2000). In the past, the IGE radar team has proposed the so-called Mountain Reference Technique (MRT) (Delrieu et al. 1997; Serrar et al. 2000; Bouilloud et al. 2009) to take advantage of this drawback for both correcting for attenuation and performing a self-calibration of the radar. The idea was to estimate path-integrated attenuations (PIA) in some specific directions from the decrease of mountain returns during rainy periods. Such PIA estimates were then used as constraints for backward or forward attenuation correction algorithms (Marzoug and Amayenc 1994) with optimization of an effective radar calibration error, given a drop size distribution (DSD) parameterization. The development of polarimetric radar techniques (e.g. Bringi and ~~Chandrasakar~~Chandrasekar 2001; Ryzhkov et al. 2005) has allowed a scientific breakthrough for quantitative precipitation estimation (QPE) at X-band by exploiting the relationship which exists between the specific differential phase ~~(K_{dp}~~shift on propagation (K_{dp}, in ° km^{-1}) and the specific attenuation ~~k~~k (dB km^{-1}). ~~Similarly to~~As with the MRT, the differential propagation phase ~~$\Phi_{dp}(r_2) - \Phi_{dp}(r_1)$~~$\Phi_{dp}(r_2) - \Phi_{dp}(r_1)$ over a given path ~~(r_1, r_2)~~(r_1, r_2) can be used to estimate ~~$PIA(r_1, r_2)$~~$PIA(r_1, r_2)$, which can ~~be used to~~ constrain a backward attenuation correction algorithm and allow a self-calibration of the radar and/or an adjustment of the DSD parameterization (Testud et al. 2000; Ryzhkov et al. 2014). Two major advantages of the polarimetric technique over the MRT can be formulated: (1) the availability of PIA constraints for any direction with significant precipitation and (2) the subsequent possibility to use a backward attenuation correction algorithm, which is known to be stable while the forward formulation is essentially unstable. Accounting for their respective potential in different rain regimes (moderate to heavy), some combined algorithms making use of various polarimetric observables (reflectivity, differential reflectivity and specific differential phase shift on propagation) have also been proposed for the X-Band frequency (e.g. Matrosov and Clark, 2002; Matrosov et al. 2005; Koffi et al. 2014). Although the polarimetric

QPE methodology is now quite well established and validated for rainy precipitation (Matrosov et al., 2005; Anagnostou et al. 2004; Diss et al. 2009), Yu et al. (2018) point out, in their first performance assessment of the RHyTMME radar network, (i) the need to better understand and quantify attenuation effects in the melting layer (ML), (ii) the importance of non-uniform beam filling (NUBF) effects at medium to long ranges in such a high-mountain context, as well as (iii) the stronger impact of radome attenuation at X-band compared to S- or C-Band.

Since 2016, we have the opportunity to operate a research X-Band polarimetric radar system (XPORT radar hereinafter) at IGE at the bottom of the Grenoble valley. This unique facility, consisting of two radar systems 11 km apart operating on an altitudinal gradient of about 1700 m, should enable us to make progress on how to deal with the altitude dilemma and with potential / issues associated with the choice of the X-band operating frequency. Following a first article based on the RadAlp experiment about the characterization of the melting layer (Khanal et al. 2019), we concentrate hereinafter on the relationship between total differential phase ~~($\boldsymbol{\phi_{dp}}$~~shift (ϕ_{dp}) derived from polarimetry and PIA derived from the MRT. In section 2, we present the observation system available, as well as ~~the two~~ contrasted rainy events considered in this study: (i) a set of nine convective ~~case~~events with ~~strong rainrates~~high rain rates, for which the melting layer was well above the detection domain of the XPORT radar, allows us to study the ~~$\boldsymbol{\phi_{dp} - PIA}$~~$\phi_{dp} - PIA$ relationship in rain; (ii)~~ during~~ a stratiform case with moderate rainrates, for which the melting layer rose up from about 1000 m asl up to 2500 m asl, ~~we were able~~allows us to perform a horizontal scanning of the ML with the MOUC radar and a ~~detailed~~preliminary analysis of the ~~$\boldsymbol{\phi_{dp} - PIA}$~~$\phi_{dp} - PIA$ relationship in the various layers of the ML. We present and illustrate in section 3 the methodology used for the PIA and ~~$\boldsymbol{\phi_{dp}}$~~ϕ_{dp} estimation. We also investigate ~~in section 3~~ the relationship between the specific differential phase ~~($\boldsymbol{K_{dp}}$~~shift on propagation (K_{dp}) and the specific attenuation (~~$\boldsymbol{k}$~~k) thanks to drop size distribution (DSD) measurements collected in the Grenoble valley during the two sets of events. The results concerning the ~~$\boldsymbol{\phi_{dp} - PIA}$~~$\phi_{dp} - PIA$ relationship in rain and in the ML are presented and discussed in section 4, while conclusions and perspectives are drawn in section 5.

2. Observation system and datasets

2.1. Observation system

Grenoble is a Y-shaped alluvial valley in the French Alps with a mean altitude of about 220 m asl surrounded by three mountain ranges: Chartreuse (culminating at 2083 m asl) to the north, Belledonne (2977 m) to the south-east and Vercors (2307 m) to the west. Figure 1 shows the topography of the area as well as the positions of the Météo-France radar system on top of the Mt Moucherotte and the IGE experimental site at the bottom of the valley.

Figure 1 here

Among other devices, the ~~IGE33~~IGE experimental site includes: (i) the IGE XPORT research radar ~~[13],~~(Koffi et al. 2014); see Table 1 for the list of its main parameters; (ii) one micro-rain radar (MRR, not used in the current study~~),~~ (iii) one

meteorological station including pressure, temperature, humidity, wind probes and several raingauges, (iv) one PARSIVEL2 disdrometer. The characteristics of the MOUC radar are listed in Table 1 ~~as well~~. XPORT radar was ~~constructed~~built in the laboratory in the 2000s. It was operated during more than 10 years in Western Africa within the AMMA and Megha Tropiques Cal-Val campaigns. Since its return in France in 2016, a maintenance and updating program is underway to improve its functionalities, notably with respect to the real time data processing and the antenna control program. One noticeable feature for XPORT radar is the range bin size of 34.2 m (corresponding actually to an over-sampling since, for a pulse width of 1 µs, the theoretical bin size is 150 m) which is an interesting figure for the close range and ~~volumic~~volumetric measurements considered in this study. Note that while the MOUC radar is operated 24 hours a day and its data integrated in the Météo France mosaic radar products, the XPORT radar is operated on alerts only for significant precipitation events.

2.2 Dataset

Table 2 ~~gives the list of~~shows the main characteristics of nine convective events considered for the study of the ~~$\boldsymbol{\phi_{dp} - PIA}\phi_{dp} - PIA$~~ relationship in rain, by using the XPORT radar data. ~~The~~A stratiform event, which occurred on January 3-4, 2018, ~~will be~~is also considered for a preliminary study of the ~~$\boldsymbol{\phi_{dp} - PIA}\phi_{dp} - PIA$~~ relationship in the ML, with both the MOUC and the XPORT radar data. Figure 2 presents time series of one of the most intense convective event (July 21, 2017) and the stratiform event. In both cases, the total rain amount observed at the IGE site was about 35 mm, but in 3 hours with two peak rainrates of about 40 mm h^{-1} for the July 21, 2017 convective event while the January 3-4, 2018 stratiform event lasted more than 12 hours with an average rainrate of about 3 mm h^{-1}. The two events also differ by their vertical structure. The bottom graphs of Fig. 2 display the time series of the altitudes of the tops, peaks and bottoms of the horizontal reflectivity (Zh) and co-polar correlation coefficient (~~$\boldsymbol{\rho_{hv}}\rho_{hv}$~~) signatures of the ML, ~~derived from~~obtained with the automatic detection algorithm described in Khanal et al. (2019). The quasi-vertical profiles (QVP, Ryzhkov et al. 2016) derived from the XPORT 25°-PPIs are considered in the ML detection. For the convective case, the ~~melting layer~~ML extends from 3000 up to 4000 m asl and more, i.e. well above the altitudes of the two radars. Table 2 indicates this is also the case for the other convective events~~.~~, at least for the XPORT radar. For the stratiform event, the ML extends between 800 and 1500 m asl during the first part of the event (between January 3 20:00 UTC to January 4 01:30 UTC) and then rises in about 2 hours to stabilize at an altitude range of about 2200-2800 m asl after 04:00 UTC, passing progressively at the level of the MOUC radar in the meantime.

Figure 2 here

~~In the following, we will consider the XPORT radar measurements at the elevation angle of 7.5° and the MOUC radar measurements at the elevation angle of 0° to study the $\phi_{dp} - PIA$ relationship in rain and in the ML, respectively.~~

As an additional illustration of the dataset, Fig. 3 gives two examples of XPORT PPIs at 7.5° elevation angle for moderate (left) and intense (right) rain during the July 21, 2017 event. As a clear feature, one can see that, for this elevation angle, the radar beam is fully blocked by the Chartreuse mountain range in the northern sector. Also visible in the north-east sector and, to a lesser extent, in the south-west sector are ~~the~~ partial beam blockages associated with tall trees in the vicinity of the XPORT radar on the Grenoble campus. This figure is ~~mostly~~also intended at drawing the attention of the reader on the decrease on the Chamrousse and Moucherotte mountain returns (within red circles) during the intense rain time step compared to their values in moderate rain, as a first illustration of the MRT principle.

Figure 3 here

3. Methodology

Our aim is to study the relationship between two radar observables of propagation effects at X-Band: path-integrated attenuation and differential propagation phase due to precipitation occurring along the radar path. We describe in the following two sub-sections the estimation methods that were implemented. In sub-section 3.3, we complement the methodology description by ~~ground-based~~ the presentation of DSD–derived $k - K_{dp}$ relationships ~~between variables of interest~~.

3.1. Path-integrated attenuation estimation

Let us express the PIA (in dB) at a given range r (km) as:

$$PIA(r) = PIA(r_0) + 2\int_{r_0}^{r} k(s)\, ds \quad (1)$$

where $k(s)$ (dB km^{-1}) is the specific attenuation due to rain at range s (km). r_0 is the range where the measurements start to become exploitable, i.e. the range where measurements are free of ground clutter associated with side lobe effects. The term $PIA(r_0)$ represents the so-called on-site attenuation resulting from radome attenuation and range attenuation at range closer than r_0. Note that PIAs can be obtained from eq.1 for both the horizontal and the vertical polarizations. In the present article, we will restrict ourselves to the horizontal polarization, the study of differential attenuation being a possible topic for a future study. Delrieu et al. (1999) have proposed an assessment of the quality of PIA estimates from mountain returns by implementing a receiving antenna in the Belledonne mountain range in conjunction with an X-band radar operated on the Grenoble campus. ~~Basically, they~~They found a good agreement between the two PIA estimates for PIAs exceeding the natural variability of the mountain reference target during dry weather. They recommended using strong mountain returns (greater than e.g. 50 dBZ during dry weather) so as to minimize the impact of precipitation falling over the reference target itself. They also point out that this approach is not able to separate the effects of on-site and range attenuation. They verified however, by implementing the receiving antenna close to the radar (at a range of about 200 m), that the on-site attenuation was negligible for a radomeless radar, which is the case for the XPORT radar but not for the MOUC radar. Another interesting feature of the MRT PIA estimator is its independence with respect to eventual radar calibration errors.

In the current study, we used the following procedure to determine the mountain reference targets for the XPORT radar:

A large series of raw reflectivity data ~~(not corrected for attenuation),~~ observed during widespread rainfall with no ML contamination, was accumulated and averaged in order to characterize the detection domain of the XPORT radar at the 7.5° elevation angle. This allowed us to determine the mountain returns, the full beam blockages due to mountains, the partial beam blockages due to tall trees~~,~~ as well as spurious detections due to side-lobes~~,~~ in the vicinity of the radar. A manual selection of the mountain reference targets was then performed based on the map of the apparent reflectivity~~, thresholded at~~ above 45 dBZ. The targets, made of mountain returns from successive radials (up to 9) with a limited range extent (less than 2.~~8~~0 km), are described in Table 3. Based on the radar equation and the receiver characteristics, care was taken to discard ~~range gates~~targets eventually subject to saturation~~.~~ at close range. The selected targets ~~have~~ are located at a mean range comprised between 4.1 and 17.1 km, and have sizes between 0.06 and 0.94 km². ~~Then, for~~For each ~~considered~~ rain ~~events~~event, dry-weather data before and/or after the event ~~was considered~~were used to characterize the mean target reflectivity and its time variability. Note that the mean reflectivity for each target and each time step was computed as the average of the dBZ values of each radial gate composing the target. This is justified by the fact we aim at estimating PIAs in dB. Table 3 lists the mean, standard deviation, 10 and 90% quantiles of the ~~distribution~~time series of the dry-weather apparent reflectivity of the reference targets for the first and ~~the~~ last ~~events~~event of the considered series. One can notice the ~~remarkable~~good stability of the mean reflectivity values between the two events, an indication of both the radar calibration stability during the ~~considered~~ period and a moderate impact of the mountain surface conditions, already evidenced in previous studies (e.g. Delrieu et al. 1999; Serrar et al. 2000) in similar mountainous contexts. ~~In addition, the~~The standard ~~deviation~~deviations of the reflectivity time series ~~appears low, in the~~ range ~~of~~between 0.2 to 0.9 dBZ, and the mean 10-90% inter-quantile range is equal to 1.03 dBZ.

Due to limited data availability, a simpler approach was implemented for the selection of the MOUC mountain reference targets. Here again, the raw reflectivity data were accumulated and averaged, but only over the period January 3rd, 2018, 19:00 – 23:55 UTC preceding the rise of the ML at the level of the MOUC radar. It was snowing during this period at the MOUC radar site. So, we are implicitly making the assumption of negligible attenuation during snowfall (supported in the literature, e.g. Matrosov et al. 2009) in the considered case study. Table 4 displays the geometrical characteristics of the targets, as well as the mean, standard deviation, 10% and 90% quantiles of their apparent reflectivity time series. Targets are located at greater distances than those of the XPORT radar, i.e. between 19.9 and 44.9 km. In spite of having larger sizes (between 0.7 and 4.0 km²), this range effect probably explains their standard deviations to be higher, between 0.75 and 1.44 dBZ. The 10-90% inter-quantile ranges are subsequently higher as well, with a mean value of 2.6 dBZ.

The top graphs of Fig. 4 give two examples of apparent reflectivity profiles for a radial of a given target, during the July 21st, 2017 rain event. The example on the left side corresponds to a moderate PIA (5.4 dB when considering all the gates of the radials composing the target) and the right-side example corresponds to one of the highest PIA value observed (27.6 dB) in our dataset. We tried to limit as far as possible the radial extent of targets (less than 2000 m) and/or multi-peaks targets, such

as the one shown on the left-side example, in order to limit positive bias on MRT PIA estimates. The top graphs of Fig. 5 give two examples of apparent reflectivity time series during the events of July 21st, 2017 and July 20th, 2018, together with the mean, 10% and 90% quantiles of the dry-weather apparent reflectivity. For both cases, the XPORT data acquisition started a bit after the actual beginning of the storm. Therefore, the dry-weather reference values were estimated with data collected after the event, between 19:00 and 22:00 UTC for the July 21st, 2017 event and between 00:00 and 06:00 UTC the day after for the July 20th, 2018 event. For these convective events, one can note the erratic nature of the apparent reflectivity time series at the XPORT radar acquisition period used at that time (about 7 min). The MRT PIA estimates are simply calculated as the difference between the mean values of the target apparent reflectivity during dry-weather and at each time step of the rain event (blue lines in the bottom graphs of Fig. 5).

Figure 4 here

Figure 5 here

3.2. Differential propagation phase estimation

Let us express the total differential ~~propagation~~ phase shift between co-polar (hh and vv) received signals as:

$$\psi_{dp}(r) = 2 \int_{r_0}^{r} K_{dp}(s)\, ds + \delta_{hv}(r) \quad (2)$$

where $K_{dp}(s)$ is the specific differential phase shift on propagation [° km^{-1}] related to precipitation at any range s between r_0 and r, and $\delta_{hv}(r)$ is the differential phase ~~upon scattering~~shift on backscatter [°] at range r.

The quantity of interest, the differential propagation phase associated with precipitation along the path, is denoted:

$$\phi_{dp}(r) = 2 \int_{r_0}^{r} K_{dp}(s)\, ds = \psi_{dp}(r) - \delta_{hv}(r) \quad (3)$$

~~Like~~As with the on-site attenuation for the MRT technique, we have here a problem with the possible influence of the differential phase ~~upon scattering~~shift on backscatter $\delta_{hv}(r)$ that may introduce a positive bias on the estimation of the differential ~~propagation~~ phase shift associated with precipitation along the path. We find in the literature (e.g. Otto and Russenberg 2011; Schneebeli and Berne 2012) power-law relationships between δ_{hv} and Z_{dr} at X-band in rain, giving values for ~~backscattering~~ differential phase shift on backscatter in the ranges of [0.6° – 1.0~~]~~°] and [2.1° – 3.5~~]~~°] for differential reflectivity of 1 and 2 dB, respectively. Scattering simulations based on disdrometer data (Trömel et al. 2013) indicate that there ~~is~~may exist quite a large scatter with respect to such power-law models and an important influence of the considered hydrometeor temperature. ~~Keeping this problem and the related orders of magnitude in mind, we will consider in this preliminary study ψ_{dp} to be an estimator of ϕ_{dp}. In other words we will suppose δ_{hv} to be negligible~~From simulations based on radar data at various frequencies, the same authors quantify δ_{hv} values as high as 4° in the ML at X-Band. An anonymous reviewer of this article also mentioned that strong δ_{hv} values may be associated with hail; let us note that no hail was reported

for the convective cases considered in the present study. Keeping the related orders of magnitude in mind and the fact that significant δ_{hv} effects are associated with "bumps" in the ψ_{dp} profiles, we will carefully discuss hereafter the possibility to assume δ_{hv} to be negligible or not with respect to ϕ_{dp}.

~~Other difficulties in the ϕ_{dp}~~ In this study, the following method was implemented for the processing of the ψ_{dp} profiles and the subsequent estimation ~~are~~ of ϕ_{dp} values near the mountain targets for the XPORT radar (rain case based on convective events):

We first determined so-called "rainy range gates" along the path by using the ρ_{hv} profiles. The raw $\psi_{dp}(r)$ values for which $\rho_{hv}(r)$ was less than 0.95 (empirical threshold) were set to missing values. In addition, we defined the beginning of the rainy range by determining the first series of 10 successive gates (empirical choice, corresponding to a range extent of 342 m) overpassing this threshold. The r_0 value was set to the minimum range value of this series. Similarly, we defined the end of the rainy range by determining the last series of 10 successive range gates overpassing this threshold close to the mountain target. A maximum rainy range, denoted r_M, was defined as the maximum range value of this series. It is noteworthy to mention that rain likely occurs in the ranges less than r_0 and greater than r_M, as well as in ~~identifying the~~ the intermediate ranges for which the $\psi_{dp}(r)$ values were set to missing values. It is however critical to discard such gates that may be prone to clutter due to side lobes close to the radar or to mountain returns close to the mountain target. Although the intermediate missing values will not impact the ϕ_{dp} estimation, we have to mention that both the initial and final missing values may result in a negative bias on the PIA estimation based on $\phi_{dp}(r_M)$.

In the current version of the procedure, every single radial was processed separately. First, an unfolding was applied by adding 360° to negative $\psi_{dp}(r)$ values. The system differential phase ~~and in dealing with the noise affecting the ψ_{dp} measurements. The system differential phase~~shift was estimated ~~by~~as the median ~~value~~ of the ~~raw~~ ψ_{dp} ~~profile over~~(r) values corresponding to the ~~N closest rainy rain gates (see below for the determination~~beginning of the rainy range ~~gates), with $N=10$ for XPORT radar, i.e. a range extent of 342 m~~. This value was substracted to the raw $\psi_{dp}(r)$ profiles, and ~~$N= 4$ for MOUC radar, i.e. a range extent of 960 m~~eventual negative values were set to 0. Regarding the ψ_{dp} measurement noise processing, we have implemented and improved a regularization procedure initially proposed by Yu and Gaussiat (2018~~) which~~). This procedure consists in defining an upper envelope curve, starting from r_0, and a lower envelope curve ~~of the measured ψ_{dp} profile that are progressively brought together by an iterative elimination of anomalous ψ_{dp} jumps from one range gate to the next. In~~, starting from r_M, by considering a ~~final step, the~~ maximum jump, denoted *diffmax*, authorised between two successive gates. The calculation was performed for a series of *diffmax* values in the range of 0.5 – 10°. The regularized ψ_{dp} ~~profile~~profiles (increasing monotonous ~~curve) is~~curves) were estimated by taking the average of the upper and lower envelope curves. ~~Such an algorithm may be efficient to~~ Note that the values for the missing gates between r_0 and r_M were simply interpolated with the adjacent values of the regularized profile. A mean absolute difference criterion (MAD) between the raw and regularized

profiles over a series of 30 gates with non-missing values near the mountain target (empirical choice, corresponding to a range extent of about 1 km) was used to determine the optimal *diffmax* value and the associated profile. The optimal profile was finally selected if the MAD criterion was less than 50%, otherwise we considered the polarimetry-derived PIA to be missing for the considered radial. Finally, the $\Phi_{dp}(r_M)$ value for the target was estimated as a weighted average of the $\Phi_{dp}(r_M)$ values of all the non-missing radials composing the target, the weights being the number of reference gates of each radial. The bottom graphs of Fig. 4 present the raw and regularized profiles, as well as the envelope curves, for the examples already commented above. For the right-hand example corresponding to one of the strongest PIA (27.6 dB) observed, one can note that the noise of the raw Ψ_{dp} profile is low, especially in the range with the highest gradients between 7 and 13 km. There is no apparent "bump" on the raw profile that could sign a δ_{hv} contamination; so that one might be tempted to consider the regularized profile as a good estimator of the Φ_{dp} profile in that case. The left-hand side example, corresponding to a moderate MRT-derived PIA of 5.4 dB, is more complex. As already noted, the mountain target itself is noisy with significant mountain return contamination before range r_M as evidenced by the ρ_{hv} profile. In addition, one can note a non-monotonic behaviour of the raw Ψ_{dp} profile with a plateau of about 17.5° for ranges greater than 4 km, following an increase in the raw profile (with moderate noise) up to 22° at 4-km range. One might assume a δ_{hv} contamination in that case. Interestingly, the regularisation procedure is shown to provide a good filtering of the "bump", and here again we are tempted to consider the regularized profile as a good estimator of the Φ_{dp} profile. The middle graphs in Fig. 5 display the time series of the $\Phi_{dp}(r_M)$ values associated with the apparent reflectivity of mountain returns discussed above. One can note a good consistency of the two time series for the highest peaks while discrepancies can be evidenced for the moderate and small values.

Basically, the same methodology was implemented for the MOUC radar case study, with some ~~extent~~alterations to ~~filter nonmonotonic behaviour of the Ψ_{dp} profile associated with contribution from δ_{hv}.~~

~~For both the PIA and Ψ_{dp} estimators, it was found necessary to determine so-called rainy range gates along the path, especially to determine the r_0 value and a range value close to the reference target, denoted r_M, for which the Ψ_{dp} values are not affected by mountain clutter. For this purpose, we considered a given range gate as rainy if $Z_h \geq 15\ dBZ$ and $\rho_{hv} \geq 0.95$ for rain profiles. We had to suppress the ρ_{hv} constraint for profiles passing through the melting layer, due to the well-known decrease of ρ_{hv} in the ML (Khanal et al. 2019).~~

be described hereafter. Figure ~~4 illustrates the PIA and Φ_{dp} estimation method for a given mountain target for the measurements of the 7.5° PPI of the XPORT radar for two~~ 6 provides the time ~~steps during the convective event of July 21, 2017. The selected target at range 14 km (top graph) comprises a~~ series of ~~successive gates with dry-weather mean reflectivity value greater than 45 dBZ. The raw reflectivity profiles exhibit a decrease of about 5 and 20 dB compared to the dry-weather returns at the reference target range. The measured Ψ_{dp} profiles (middle) are comparatively noisier in weak precipitation. The regularization procedure is illustrated with the display of the two envelope curves. The resulting~~

~~increasing monotonous curves provide good fits to the raw profiles, with ψ_{dp} estimates of 12 and 60° near the reference mountain target for the two examples. The ρ_{hv} profiles (bottom graphs) confirm that rain is present on the entire profiles and they allow to detect clutter at close range and for the mountain reference target. Note that the ρ_{hv} perturbations in the region of the mountain target are less pronounced for the case with more intense precipitation (right), probably as the result of heavier rain falling over the mountain itself.~~

~~*Figure 4 here*~~

~~Figure 5 provides another illustration of the methodology with the time series of (a)~~ the apparent reflectivity of a given mountain target, ~~(b)~~ the resulting PIA estimates~~,~~ and ~~(c)~~ the ~~ψ_{dp}~~ $\phi_{dp}(r_M)$ estimates for the 0°-PPI of the MOUC radar during the stratiform event of January 3-~~4~~4th, 2018. The time period considered in the figure ranges from 00:00 UTC to 06:00 UTC on January 4th, 2018 in order to focus on the rising of the ML between 02:00 UTC and 04:00 UTC. The ~~considered~~ target is located at ~~distances comprised between 26.4 and 29.7~~a distance of 19.9 km from the radar. The bottom ~~plot (d)~~graph of Fig. ~~5~~6 displays the results of the ML detection algorithm (Khanal et al. 2019) in terms of the altitudes of the top, peak and bottom of the Z_h (blue) and the ρ_{hv} (orange) ML signatures. The altitude of the Z_h top inflexion point is assumed to correspond to the 0°C isotherm altitude while the ρ_{hv} bottom inflexion point corresponds well with the bottom of the ML according to Khanal et al. (2019). We therefore define the ML width as the altitude difference between Zh top and ρ_{hv} bottom.

Before 02:00 UTC, the ML is well below the altitude of the MOUC radar. MOUC radar measurements at the 0°-elevation angle are therefore made in snow/ice precipitation during this period. Based on the ML detection results, the passage of the ML at the altitude of the MOUC radar begins at about 02:20 UTC and ends at 04:10 UTC. After this time, MOUC radar measurements are therefore made in rainfall. ~~Assuming attenuation at X-band to be negligible in snow, we consider the average of the apparent reflectivity of the mountain reference target between 00:00 UTC and 02:00 UTC (horizontal red line in Fig. 5a) as the dry-weather reference value required for our PIA estimations. During this period, the PIA is subsequently set to 0. The mean value of $\psi_{dp}(r_M)$ is equal to 12.3°, resulting in a specific differential phase of 0.22 °km^{-1} if the differential phase upon scattering~~

Figure 6 here

As representative examples, Fig. 7 illustrates range profiles taken by the MOUC radar during the snowfall (left) and the ML (right) periods. As expected, the ρ_{hv} profiles are very different in the two cases, with ρ_{hv} values close to 1 in snow indicating precipitation homogeneity while ρ_{hv} presents a high variability in the ML. During the ML period, we had therefore to adapt the ρ_{hv} threshold used to detect gates with precipitation. Based on the ρ_{hv} peak statistics presented by Khanal et al. (2019),

we have chosen a value of 0.8. As it can be seen in Fig. 7, such a threshold may prevent detection of the mountain reference return itself. Subsequently, we had to adapt the determination of ranges r_0 and r_M with respect to the XPORT radar case, firstly by considering two successive gates corresponding to a range extent of 480 m (instead of 10 gates, corresponding to 342 m) and secondly by making sure that the calculated r_M value was less than the range of the first mountain reference gate. Regarding the regularization of the ψ_{dp} profiles (bottom graphs of Fig. 7), it was found that the raw profiles were noisier compared with the XPORT case study. Well-structured "bumps" were not evidenced in the ML profiles, maybe as a result of the lower range resolution of the MOUC radar, and the regularisation procedure was found to work satisfactorily. It remains however difficult to assume that there is no δ_{hv} contamination during the ML period.

Figure 7 here

Coming back to Fig. 6, one can note the mean value of $\phi_{dp}(r_M)$ to be equal to 11.2° during the snowfall period, resulting in a specific differential phase shift on propagation of 0.28 °km^{-1} if the differential phase shift on backscatter is neglected. Such values indicate a significant heterogeneity of the horizontal and vertical dimensions of the snow/ice hydrometeors.

During the rainy period between 04:10 and 06:00 UTC, there is a good coherence between the specific attenuations derived from the MRT PIA (0.078 dB km^{-1} at around 04:00 UTC - 0.035 dB km^{-1} at 06:00 UTC) and those derived from the polarimetry (0.076 - 0.046 dB km^{-1} at the same time steps) using ~~*Figure 5 here*~~

~~During the other two periods, the PIA is simply estimated as the difference between the dry-weather reference value and the apparent reflectivity of the mountain target at the considered time step. Note that a slightly more sophisticated method has been proposed in [7] to determine the dry-weather base line by considering the reference target reflectivity before and after precipitation, in an attempt to account for possible effects of the wetting of the mountain surfaces. The reference mountain returns do not exhibit significant differences before and after precipitation (not shown in Fig. 5 since we concentrate on the period of ML rising), which justifies the simple method used in this study. During the rainy period after 04:10 UTC, the average PIA is 3.3 dB, corresponding to an average specific attenuation of 0.059 dB km^{-1}. This estimate is rather high (overestimation of 37%) if compared with the specific attenuation estimate derived from the $k - R$ relationship proposed by Delrieu et al. (1991) for widespread rainfall at X-Band for a temperature of 0°C: $k = 1.05\ 10^{-2}\ R^{1.15}$. This empirical relationship yields $k = 0.037$ dB km^{-1} for $R = 3$ mm h^{-1}; the latter value being the average rainrate observed at the IGE site between 04:00 UTC and 06:00 UTC. The average $\psi_{dp}(r_M)$ value during the same period is 9.7°, corresponding to a mean K_{dp} value of 0.173 °km^{-1} if the differential phase upon scattering is neglected. Using~~ the $k - K_{dp}$ relationship established for this event by using the DSD measurements available at the IGE site (see section 3.~~2 below), one obtains a k value of 0.036 dB km^{-1}, in remarkable agreement with the k estimate derived from the $k - R$ relationship for widespread rainfall.~~

~~These simple calculations have to be considered with caution. However, they suggest a slight PIA overestimation of about 1 dB during the rainy period, which could be well associated with radome attenuation of the MOUC radar.~~3 below).

Our main objective with the January 3-~~4~~4th, 2018 event is to study the $\phi_{dp} - PIA$ relationship within the ML. Figure ~~5 clearly~~6 indicates that both variables take, as expected, higher values during that period compared to during the ~~snow~~snowfall and the ~~rainy~~rainfall periods. The maximum values reached are ~~13.1~~14.2 dB for PIA and ~~23.0~~25.6° for ~~Ψ_{dp}~~$\phi_{dp}(r_M)$. Figures ~~5b~~6b and ~~5c~~6c also show that the co-fluctuation of the two time series is not that good during the ML period with a ~~Ψ_{dp}~~$\phi_{dp}(r_M)$ signal having a trapezoidal shape with maximum values between 02:35 UTC and 03:15 UTC while the MRT PIA signal is more triangular and peaks at 03:15 UTC. We note that the two signals compare well after the peak and that they both peak down at ~~around 04:00~~03:55 UTC when measurements are made in the lowest part of the ML. These features are quite systematic for all the ~~sixteen~~thirteen targets considered for the MOUC radar for this event, giving the impression that the $\phi_{dp} - PIA$ relationship depends on the position within the ML and as such on the physical processes occurring during the melting. ~~This point will be further illustrated and discussed in sub-section 4.2.~~ This will be further illustrated and discussed in sub-section 4.2. However, we have to mention here three points that may limit the validity of such inferences for the MOUC radar configuration compared to the XPORT one: (i) the MRT PIA estimates may be positively biased by radome attenuation, (ii) the polarimetry – derived PIA estimates may be affected by δ_{hv} contamination in the ML and (iii) non-uniform beam filling effects become probably significant for the 20-40 km range considered, leading to a smoothing of the radar signatures. There is no evidence so far of the first two points in the available dataset; this may be due to the moderate intensity of this precipitation event.

3.3. Study of the $k - K_{dp}$ relationship in rain from in-situ DSD measurements

Before presenting the analysis of the $\phi_{dp} - PIA$ relationship in rain and in the melting layer based on the estimates for all the mountain targets and time steps available for the two sets of events, we study in this sub-section the $k - K_{dp}$ relationships that we were able to derive from the DSD measurements collected at ground level at the IGE site. For ~~both~~all the events, precipitation was in the form of rainfall at this altitude. As for the scattering model, we used the CANTMAT version 1.2 software programme that was developed at Colorado State University by C. Tang and V.N. Bringi. The raw PARSIVEL2 DSD measurements have a time resolution of 1 min. The volumetric concentrations were computed with a 5-min resolution and binned into 32 diameter classes with increasing sizes from 0.125 mm up to 6 mm. The CANTMAT software uses the T-Matrix formulation to compute radar observables such as horizontal reflectivity, vertical reflectivity, differential reflectivity, co-polar cross-correlation, specific attenuation, specific phase shift, etc, as a function of the DSD, the radar frequency, air temperature, oblateness models (e.g. Beard and Chuang 1987; Andsager et al. 1999; Thurai and Bringi 2005) and canting models for the rain drops as well as the incidence angle of the electromagnetic waves. Figure ~~6~~8 displays

the empirical $k - K_{dp}$ pairs of points obtained for the ~~two~~convective events (left) and the stratiform one (right) as well as the fits of least-square linear models and power-law non-linear regressions.

~~*Figure 6 here*~~

Figure 8 here

Based on the literature review mentioning an almost linear relationship between k and K_{dp} at X-Band (Bringi and ~~Chandrasakar~~Chandrasekar, 2001; Testud et al. 2000; Schneebeli and Berne 2012) we have first tested a linear regression with an intercept forced to be equal to 0 (red ~~line~~lines in Fig. ~~6~~8). This simple model indeed provides a rather good fit to the data, especially for the convective ~~event~~events. Due to the observed bending of the scatterplots, we have also tested a non-linear regression to a power-law model (blue curve) which significantly improves the fittings. A sensitivity analysis was performed in order to test the influence of the raindrop temperature, the raindrop oblateness model, the standard deviation of the canting angle distribution, the incidence angle. For reasonable ranges of variation of these parameters, the DSD itself appears to be the most influent factor on the values of the regression coefficients. We note that the slopes of our 0-forced linear models are significantly higher than values proposed in the literature (0.233 in ~~[10];~~Bringi and Chandrasekar (2001); 0.205 – 0.245 in ~~[19]).~~Scheebeli and Berne (2012)). The exponents of the fitted power-law models are also significantly higher than 1.0. The fits in Fig. ~~6~~8 correspond to the most likely parameterization of the scattering model in terms of temperature and incidence angles for the two events, i.e. 20°C and 7.5° respectively for the convective ~~case~~cases and 0°C and 0° for the stratiform case. The Beard and Chuang (1987) formulation was used as the raindrop oblateness model. The DSD-derived linear and non-linear k - K_{dp} relationships were used to process the regularized $\phi_{dp}(r)$ profiles which were first simply derivated to obtain the $K_{dp}(r)$ profiles prior to the application of the two k - K_{dp} relationships. The bottom graphs of Fig. 5 shows examples of the resulting polarimetry-derived PIAs.

4. Results

4.1. Study of the ~~ψ_{dp}~~ϕ_{dp} – PIA relationship in rain

Figure ~~7~~9 displays the scatterplot of the ~~ψ_{dp}~~$\phi_{dp} - PIA$ values obtained for the ~~July 21st, 2017~~nine convective ~~event~~events (Table2) with the XPORT 7.5°-PPI data, following the methodology described in ~~section~~sections 3.1 and 3.2. The data from the sixteen mountain targets~~, situated between 4 and 16 km from the XPORT radar,~~ (Table 3) were considered. ~~We took care to discard~~For a given event, targets ~~leading to receiver saturation at closer ranges. Pairs of points for which~~with maximum

MRT ~~PIA estimates were~~ derived PIAs less than ~~1~~5 dB were discarded ~~as well to account for the temporal variability of the dry weather mountain returns. This threshold can be seen as a sensitivity~~ in order to limit ~~of~~ the ~~MRT~~weight of small PIA ~~estimator~~estimates in the global analysis. Since we consider the two variables on an equal footing, we preferred to calculate the least-rectangles regression (blue straight line) between the two variables rather than the least-squares regression of one variable over the other one. One can notice the rather large dispersion of the scatterplot, with explained variance of ~~72%. Quite remarkably,~~77%. We note the regression slope (0.~~44) is relatively close to~~41) to be higher than the slope of the $k - K_{dp}$ linear relationship (0.~~353~~336), reported as the red straight line in Fig. ~~7~~9.

Figure ~~7~~9 here

To go further, Fig. ~~8~~10 presents the comparison of the MRT-derived PIAs with the polarimetry-derived PIAs. ~~For the latter, we simply calculated the derivative of the XPORT ψ_{dp} profiles and applied the $k - K_{dp}$ relationships derived from disdrometer measurements (Fig. 6 left). No attempt was made to correct the ψ_{dp} profiles for effect of the differential phase upon scattering, i.e. we assume $\phi_{dp} = \psi_{dp}$. As one could guess from examination of Fig. 7, the~~The linear $k - K_{dp}$ relationship leads to a significant positive bias for the polarimetry-derived PIAs with a least-rectangles slope of 1.~~29~~24. The non-linear $k - K_{dp}$ relationship does indeed a good job in reducing this bias (least-rectangles slope of 1.~~05).~~03). This result may be surprising given the $k - K_{dp}$ relationships displayed in Fig. 8. One has to realize that the range of K_{dp} values is much smaller for the 5-min DSD estimations than for the $K_{dp}(r)$ profiles discretized with a 34.2 m resolution. Considering the 1-min DSDs allowed us to confirm the validity of the linear and non-linear $k - K_{dp}$ models for a wider K_{dp} range (not shown here for the sake of conciseness). We are therefore confident in the relevance of the results presented in Fig. 10.

Figure 10 here

~~*Figure 8 here*~~

4.2. Study of the $\psi_{dp} - PIA$ relationship in the Melting Layer

Figure ~~9~~11 displays the scatterplot of the ~~ψ_{dp}~~$\phi_{dp} - PIA$ values obtained in the ML for the January 4th, 2018 stratiform event with the MOUC 0°-PPI data, following the methodology described in section 3.1 and 3.2. The ~~data from sixteen mountain~~results obtained for the thirteen targets~~, situated between 8 and 42 km from the MOUC radar, were~~ (Table 4) are considered~~. Note that~~ in this analysis, with no target censoring based for instance on the minimum PA observed for a ~~majority of them are located between 22 and 30 km. Here again a 1dB threshold was taken into account~~given target as ~~the sensitivity~~

limit of the MRT PIA estimatorfor the XPORT case study. One can see that the correlation between the two variables is severely degraded compared to the rain case with an explained variance of 0.41,% and a least-rectangle slope of 0.6851 dB degree^{-1} and an intercept of -6.44 dB.. The red line isrecalls the $k - K_{dp}$ linear regression determined with the DSD observed at ground level for this event (Fig. 6 right).. Clearly, the $\psi_{dp}\phi_{dp} - PIA$ relationship is different in rain and in the ML, and as suggested when commenting Fig. 56, it likely depends on the physical processes occurring during the melting.

Figure 911 here

To investigate this point, the $\psi_{dp}\ \phi_{dp}(t)r_M)$ and $PIA(t)r_M)$ values estimated during the rising of the ML at a given time t the level of the MOUC radar are represented in Fig. 1012 as a function of their position within the ML. As already noted, we define the ML width as the difference between the Zh top altitude and the ρ_{hv} bottom altitude (Khanal et al. 2019). Since the ML width significantly varies during the considered period (from 630 to 1020 m; see Fig. 58), we found necessary to scale the altitudes by the ML width. This was achieved by considering the following linear transformation of the altitudes:

$$H(t) = (h_M - h_{\rho hvB}(t))/MLw(t) \quad (4)$$

where h_M is the altitude [m asl] of the MOUC radar, $h_{\rho hvB}(t)$ is the altitude of the ML bottom at time t and $MLw(t)$ is the ML thickness at a given time t. The scaled altitude $H(t)$ [-] subsequently takes the value 0 at ML bottom and the value 1 at ML top (orange and blue thick horizontal lines, respectively, in Fig. 1012). Furthermore, in order to locate more precisely the position of the Zh and ρ_{hv} peaks within the ML, we computed their scaled altitudes at each time step, $H_{zhP}(t)$ and $H_{\rho hvP}(t)$ respectively, as:

$$H_{zhP}(t) = (h_{zhP}(t) - h_{\rho hvB}(t))/MLw(t) \quad (5)$$

and:

$$H_{\rho hvP}(t) = (h_{\rho hvP}(t) - h_{\rho hvB}(t))/MLw(t) \quad (6)$$

where $h_{zhP}(t)$ and $h_{\rho hvP}(t)$ are the altitudes of Zh peak and ρ_{hv} peak at time t. The dotted horizontal lines in Fig. 1012 represent the 10 and 90% quantiles of the timeseriestime series of the scaled altitudes of Zh peak (dotted blue lines) and ρ_{hv} peak (dotted orange lines). We can observe a shift between the Zh and ρ_{hv} characteristic altitudes, consistent with the ML climatology established by Khanal et al. (2019) who reported a shift of about 100 m in average between the two peaks. We note in Fig. 58 that this shift is visible before 02:00 UTC during the snowfall period and at the beginning of the ML rising but that it is less pronounced during the ML rising and its stabilization after 0403:00 UTC and during the rainfall period. In order

to better evidence their vertical trends, the MRT $PIA(t) - H(t)$ and $\psi_{dp}(t) - H(t)$ points(r_M) and $\phi_{dp}(r_M)$ values are presented in Fig. 1012 as a function of the scaled altitudes in the form of box plots with ana scaled altitude class of size 0.1. The number of counts in each class is indicated on the right of the graphs; it is a multiple of the number of MRT targets (1613 here). One can note that the) depending on the time occurrence of estimates in a given altitude class. The vertical sampling is not very rich, with missing classes within the ML. However thethere is clear signature for the two variables in the ML. The trends already evoked when commenting Fig.58 are confirmed: (i) the *PIA* valuesMRT PIAs peak when measurements are made at the level of the Zh and ρ_{hv} peaks; more precisely, the *PIA*PIA peak is observed for the altitude class containing the ρ_{hv} peaks (0.35 – 0.45scaled altitude class centered at 0.3); (ii) the region with maximum values is somewhat thicker for $\psi_{dp}\phi_{dp}$, encompassing a significant part of the upper ML, between the 0.3 and 0.8 in terms of scaled altitudes; (iii) the PIA tends towards its value in rain below the ML and towards 0 above the ML; (iv) ψ_{dp}scaled altitude classes; (iii) ϕ_{dp} tends towards almost similar values in average in rain (ML bottom) and snow (ML top).), (iv) the PIA tends towards its value in rain below the ML and towards 0 above the ML. One would have expected a more pronounced return towards 0 of the PIA on top of the ML. This lower than expected decrease could sign a radome attenuation; however the rainfall intensity is low for the considered event and the radome is equipped with a heating system so that accumulated snow is unlikely. It may also result from a smoothing effect related to non-uniform beam filling: with its 3-dB beamwidth of 1.28°, the angular resolution of the measurements of the MOUC radar is 447 m and 1005 m at distances of 20 km and 45 km, respectively, which correspond to the minimum and maximum ranges of the considered mountain targets.

Figure 12 here

Finally, Figure 1113 displays the evolution of the ratio of the mean of the MRT $PIA/\psi_{dp}(r_M)$ values over the mean of $\phi_{dp}(r_M)$ values as a function of the scaled altitudes. The value of the ratio below the ML (0.2733) is in remarkablerather good agreement with the slope of the linear model established between the specific attenuation k and the specific differential phase shift K_{dp} using the DSD measurements in rain available for this event (0.29;, see Fig. 6 right). The ratio linearly increases up to9). Near the -ρ_{hv} peak where it takes a , the ratio value closeis equal to 0.442. For the three classes of scaled altitude 0.7, 0.8 and 0.9, the ratio is between 0.32 and 0.38, with an apparent secondary maximum for the altitude class 0.8. Data with increased vertical resolution would be necessary to confirm or not this resultobservation, which is also visible on the PIA profile and on several $\psi_{dp}(t)\phi_{dp}$ and $PIA(t)$ timeseries time series like the ones displayed in Fig. 5. 8. Above the ML, the ratio progressively tends toward 0 in about 300 to 400 m.

Figure 1113 here

5. Summary and conclusions

We developed in this work a methodology for studying the relationship between total differential phase (~~ψ_{dp}~~shift (ϕ_{dp}) and path-integrated attenuation (PIA) at X-Band. Knowledge of this relationship is critical for the implementation of attenuation corrections based on polarimetry. We used the Mountain Reference Technique for direct PIA estimations associated with the decrease of ~~returns from~~strong mountain ~~targets~~returns during precipitation events. The MRT sensitivity depends on the time variability of the dry-weather mountain returns. The MRT PIAs may be positively biased by on-site attenuation related in particular to radome attenuation and negatively biased by the effect of precipitation falling over the reference targets. The polarimetry PIA estimation is based on the regularization of the raw ψ_{dp} profiles and their derivation in terms of specific differential phase shift (K_{dp}) profiles followed by the application of a power-law relationship between the specific attenuation and the specific differential phase shift. Such $k - K_{dp}$ ~~relationship can be~~relationships were evaluated for rain with a scattering model by using DSD measurements and an oblateness model for raindrops. The noise of the raw ψ_{dp} profiles, the possible contamination of the signal by differential shift on backscatter and the adequacy of the $k - K_{dp}$ relationship used determine the quality of the polarimetry derived PIAs. Non-uniform beam filling (NUBF) effects may also play a role. A point to emphasize is that both PIA estimators are not sensitive to an eventual radar miscalibration.

~~The~~ We presented first a rain case study ~~for the~~based on nine convective ~~storm of July 21st, 2017 indicates that~~ events observed with the XPORT radar located in the ~~relationship between MRT derived PIAs and polarimetry derived PIAs presents a considerable dispersion (explained variance of 0.72). Both methods are prone to specific errors and, even if the MRT PIA estimator is more directly related to power attenuation, it is *a priori* difficult to say which estimator is the best. In this preliminary study, we did neglect the possible impact of the differential phase upon scattering $\delta_{hv}(r)$. We remind the reader that the observed PIA~~ Grenoble valley. Sixteen mountain targets were considered with dry-weather mean apparent reflectivity greater than 45 dBZ. The stability of the apparent reflectivity of the mountain targets during the considered period were shown to be very good and the time variability of the reference returns during dry-weather preceding or succeeding the rain events to be very small with standard deviations in the range ~~is 1-30 dB while the theoretical δ_{hv} range is 0-3 dB.~~of [0.2 – 0.9 dBZ]. Since the XPORT radar is radomeless, on-site attenuation effects are most likely negligible. The impact of rain falling over the mountain targets may also be very limited due to the high reflectivity threshold considered (45 dBZ). The development of the regularization procedure of the raw ψ_{dp} profiles required a significant effort and we are confident in its ability at dealing with the measurement noise, especially for heavy precipitation. We carefully examined many raw and regularized profiles looking for possible evidence of δ_{hv} contamination during the considered convective events. We found out some profiles with rather well organised "bumps" that could sign such contaminations. The regularization procedure was adapted in order to filter such effects, with a satisfactory performance when they occur at some distance (some kilometres) from the mountain target. In addition, we remind the reader that the observed $\psi_{dp}(r_M)$ values extends up to 80° while the theoretical δ_{hv} range is 0-4 dB. The δ_{hv} effect may therefore impact the results obtained only at the margin. ~~Similarly, we assumed the on-site attenuation~~

~~to be negligible for the MRT PIA estimation, and we are confident that this is true since the XPORT radar is radomeless. In addition,~~ NUBF effects may constitute ~~a third~~an additional source of error which, although the rain ~~event was~~events were convective, should remain limited due to the short ranges considered ~~and the fact that the ML was well above the observed area. These errors on both PIA estimators will of course impact the quality of the attenuation corrections and the subsequent QPEs. An assessment exercise with respect to an independent data source (e.g. raingauge measurements) is desirable to distinguish the two PIA estimators. It is~~ . In the end, the scatterplot of the MRT PIAs as a function of the $\phi_{dp}(r_M)$ values for all the nine convective events presents an overall good coherence with however a significant dispersion (explained variance of 77%). It is interesting ~~and encouraging~~ to note that the non-linear $k - K_{dp}$ relationship derived from ~~(~~independent~~)~~ DSD measurements taken during the ~~event~~events of interest at ground level allows a satisfactory transformation of the XPORT ~~ψ_{dp} profiles~~ $\phi_{dp}(r_M)$ values into almost unbiased (although dispersed) PIA estimates. Both estimation methods are prone to specific errors and, even if the MRT PIA estimator is more directly related to power attenuation, it is *a priori* difficult to say which estimator is the best. An assessment exercise of attenuation correction algorithms, making use of both PIA estimators, with respect to an independent data source (e.g. raingauge measurements), is desirable to distinguish the two PIA estimators. In this perspective, a specific experiment is being designed within the RadAlp project and it will be implemented in the near future.

The Melting Layer case study of January 3-4th 2018 was made possible by the unique configuration of the observation system available. The study of the $k - K_{dp}$ relationship within the ML is desirable to better quantify attenuation effects in the ML with polarimetry; and one has to recognize that such relationship can still be very difficult to characterize theoretically with scattering models and particle size distributions to be collected in the ML. The XPORT radar located at the bottom of the valley allowed a ~~fine~~detailed temporal tracking of the ~~melting layer~~ML from below using quasi-vertical profiles derived from 25°-PPIs. The MOUC radar provided horizontal scans at ~~a higher~~an altitude of 1917 m asl in direction of several mountain targets during the rising of the ML in about 2 hours. From this dataset, it was possible to derive the evolution of PIA~~(t, r_M), $\psi_{dp}(t, r_M)$,~~(r_M) and ~~their~~ $\phi_{dp}(r_M)$ values as a function of the altitude within the ML. The evolution with the altitude of the ratio~~,~~ of the mean value of $PIA(r_M)$ over the mean value of $\phi_{dp}(r_M)$, as a proxy for the slope of a linear $k - K_{dp}$ relationship ~~during the ML rising and for a number of mountain targets, as a function of the altitude.~~within the ML, was also considered. Since the ML width ~~varies~~varied during the ML rising, we found necessary to scale the altitudes with respect to the ML width. The three variables considered present a clear signature as a function of the scaled altitude ~~shown in Figs 10 and 11.~~ In particular, the $PIA/$~~ψ_{dp}~~ϕ_{dp} ratio peaks at the level of the ρ_{hv} peak (somewhat lower than the Zh peak), with a value of ~~about~~ 0.~~4~~42 dB degree^{-1}, while its value in rain just below the ML is 0.~~27~~33 dB degree^{-1}. The latter value is consistent with the slope of the linear $k - K_{dp}$ relationship (0.29) established from concomitant DSD measurements at ground level. The $PIA/$~~ψ_{dp}~~ϕ_{dp} ratio remains quite strong in the upper part of the ML, between 0.32 and 0.38 dB degree^{-1}, before tending towards 0 above the ML. ~~Although the MOUC measurements were made with a 0° elevation angle, NUBF effects probably introduce some~~

~~smoothing, variable as a function of the range of the considered mountain targets: with its 3-dB beamwidth of 1.28°, we remind the vertical resolution of the measurements of the MOUC radar to be for instance of 446 m at 20 km. The δ_{hv} effect is likely to be more influent in this case compared to the rain case since the PIA range is significantly lower, with maximum PIAs of 15 dB. Radome attenuation may also affect the MRT PIA estimates during the ML rising. This effect may remain limited due to the weak rainrates observed during this event (3 mmh^{-1} at the IGE site).~~One would have expected a more pronounced return towards 0 of the PIA on top of the ML. This lower than expected decrease could sign on-site attenuation occurring at the beginning of the ML rise due to the melting of the snow eventually accumulated over the radome; this effect is probably low for the considered event since the snowfall intensity was small and since the radome is heated. It may also result from a smoothing effect related to non-uniform beam filling (angular resolution of 447 and 1005 m for the range of mountain target distances). The δ_{hv} effect is likely to be strong in the ML (up to 4°) and its relative importance may be quite high in our case study since the PIA range is significantly lower compared to the rain case study, with maximum PIAs of about 15 dB. However, we did not find evidence of δ_{hv} signatures in the raw $\psi_{dp}(r)$ profiles and we are confident in the ability of the regularization procedure to filter them in a rather satisfactory way if they eventually occur. Although the experimental configuration for the study of attenuation in the ML presents some limitations (possible radome attenuation, NUBF effects), the preliminary results presented here will be deepened by processing a dataset of about thirty stratiform events with the presence of the ML at the level of the MOUC radar.

~~The preliminary results presented in this article will be extended thanks to the datasets collected between 2016 and now, with a wider variety of precipitation events, as well as with physically based simulations. It is in particular important to assess to which extent the XPORT volumetric measurements are affected by attenuation in moderate precipitation leading to well defined ML layers, when the ML is below or at the level of the MOUC radar. These are indeed the situations for which we expect the main added value of the down-valley observations made at IGE.~~

Acknowledgements

We are grateful to P.N. Gatlin (NASA Marshall Space Flight Center, Huntsville, AL) for providing the CANTMAT version 1.2 software developed at Colorado State University by C. Tang and V.N. Bringi, who we also thank. The RadAlp experiment is co-funded by the Labex osug@2020, the Service Central Hydrométéorologique et d'Appui à la Prévision des Inondations (SCHAPI) and Electricité de France / Division Technique Générale (EDF/DTG).

References

Anagnostou, E.N., Anagnostou, M.N., Krajewski, W.F., Kruger, A., and Miriovsky, B.J.: High-Resolution Rainfall Estimation from X-Band Polarimetric Radar Measurements. J. Hydrometeor., 5, 110–128. https://doi.org/10.1175/1525-7541(2004)005<0110:HREFXP>2.0.CO;2, 2004.

Beard, K.V., and Chuang, C.: A new model for the equilibrium shape of raindrops, J. Atmos. Sci., 44, 1509-1524. https://doi.org/10.1175/1520-0469(1987)044<1509:ANMFTE>2.0.CO;2, 1987.

Andsager, K., Beard, K.V., and Laird, N.E.: Laboratory measurements of axis ratios for large raindrops. J. Atmos. Sci., 56, 2673-2683. https://doi.org/10.1175/1520-0469(1999)056<2673:LMOARF>2.0.CO;2, 1999.

Bouilloud, L., Delrieu, G., Boudevillain, B., Borga, M., and Zanon, F.: Radar rainfall estimation for the post-event analysis of a Slovenian flash-flood case: application of the Mountain Reference Technique at C-band frequency. Hydrol. Earth Syst. Sci. 13(7): 1349-1360. DOI: 10.5194/hessd-6-667-2009, 2009.

Bringi, V.N., and Chandrasekar, V.: Polarimetric Doppler weather radar, principles and applications. Cambridge University Press, 636 pp, 2001.

Delrieu, G., Caoudal, S., Creutin, J.D~~., and Saint-Andre, I.: Mean K-R Relationships: Practical Results.~~: Feasibility of using mountain return for ~~Typical Weather Radar Wavelengths.~~the correction of ground-based X-band weather radar data. J. Atmos. Oceanic Technol., ~~8, 467–476, https://doi.org/10.1175/1520-0426(1991)008<0467:MRRPRF>2.0.CO;2, 1991.~~ 14(3), 368-385 DOI: 10.1175/1520-0426(1997)014<0368:FOUMRF>2.0.CO;2,1997.

Delrieu, G., Serrar, S., Guardo, E., and Creutin, J.D.: Rain Measurement in Hilly Terrain with X-Band Weather Radar Systems: Accuracy of Path-Integrated Attenuation Estimates Derived from Mountain Returns. J. Atmos. Oceanic Technol., 16, 405–416, https://doi.org/10.1175/1520-0426(1999)016<0405:RMIHTW>2.0.CO;2, 1999.

Delrieu, G., Andrieu, H., and Creutin, J.D.: Quantification of path-integrated attenuation for X- and C-band weather radar systems operating in Mediterranean heavy rainfall. J. Appl. Meteor. , 39(6), 840-850. http://dx.doi.org/10.1175/1520-0450(2000)039%3C0840:QOPIAF%3E2.0.CO;2, 2000.

Diss, S., Testud, J., Lavabre, J., Ribstein, P., Moreau, E., and Parent du Chatelet, J.: Ability of a dual polarized X-band radar to estimate rainfall, Advances in Water Resources, 32(7), 975-985, https://doi.org/10.1016/j.advwatres.2009.01.004, 2009.

Foresti, L., Sideris, I.V., Panziera, L., Nerini, D., and Germann, U.: A 10-year radar-based analysis of orographic precipitation growth and decay patterns over the Swiss Alpine region. Q. J. R. Meteorol. Soc., 144(176), 2277-2301, DOI: 10.1002/qj.3364, 2018.

Germann, U., Galli, G., Boscacci, M., and Bolliger, M.: Radar precipitation measurement in a mountainous region. Q. J. Royal Meteorol. Soc., 132(618), 1669-1692; DOI: 10.1256/qj.05.190, 2006.

Joss, J. and Lee, R.: The Application of Radar-Gauge Comparisons to Operational Precipitation Profile Corrections. J. Appl. Meteor., 34, 2612–2630, http://dx.doi.org/10.1175/1520-0450(1995)034<2612:TAORCT>2.0.CO;2, 1995.

Khanal, A. K., Delrieu, G., Cazenave, F., and Boudevillain, B.: Radar remote sensing of precipitation in high mountains: detection and characterization of Melting Layer in French Alps, Atmosphere, 10, 784; doi:10.3390/atmos10120784, 2019.

Koffi, A.K, Gosset, M., Zahiri, E.-P., Ochou, A.D., Kacou, M., Cazenave, F., and Assamoi, P.: Evaluation of X-band polarimetric radar estimation of rainfall and rain drop size distribution parameters in West Africa. Atmospheric Research, 143, 438-461. DOI:10.1016/j.atmosres.2014.03.009, 2014.

Marzoug, M., and Amayenc, P.: A class of single and dual-frequency algorithms for rain-rate profiling from a spaceborne radar: Part 1- Principle and tests from numerical simulations. J. Atmos. Oceanic Technol., **11**, 1480-1506. http://dx.doi.org/10.1175/1520-0426(1994)011%3C1480:ACOSAD%3E2.0.CO;2, 1994.

Matrosov, S. Y., and Clark, K.A.: X-Band Polarimetric Radar Measurements of Rainfall. J. Appl. Meteor. 41(9): 941-952. http://dx.doi.org/10.1175/1520-0450(2002)041%3C0941:XBPRMO%3E2.0.CO;2, 2002.

Matrosov, S.Y., Kingsmill, D.E., Martner, B.E., and Ralph, F.M.: The Utility of X-Band Polarimetric Radar for Quantitative Estimates of Rainfall Parameters. J. Hydrometeor., **6**, 248–262, https://doi.org/10.1175/JHM424.1, 2005.

Matrosov, S.Y., Campbell, C., Kingsmill, D.E., and Sukovich, E.: Assessing Snowfall Rates from X-Band Radar Reflectivity Measurements. J. Atmos. Oceanic Technol., 26, 2324–2339, DOI: 10.1175/2009JTECHA1238.1, 2009.

Otto, T., and Russchenberg, H.W.J.: Estimation of Specific Differential Phase and Differential Backscatter Phase From Polarimetric Weather Radar Measurements of Rain, IEEE Geoscience and Remote Sensing Letters, Vol8, Issue5, 988-992, DOI: 10.1109/LGRS.2011.2145354, 2011.

Ryzhkov, A.V., Giangrande, S.E., and Schuur, T.J.: Rainfall estimation with a polarimetric prototype of WSR-88D.J. Appl. Meteor., Vol. 44, Issue 4, p502-515. DOI: 10.1175/JAM2213.1, 2005.

Ryzhkov, A. V., Diederich, M., Zhang Pengfei, and Simmer, C.: Potential utilization of specific attenuation for rainfall estimation, mitigation of partial beam blockage and radar networking. J. Atmos. Oceanic Technol., Vol. 31, p599-619. DOI: 10.1175/JTECH-D-15-00038.1, 2014.

Ryzhkov, A., Zhang, P., Reeves, H., Kumjian, M., Tschallener, T., Trömel, S., and Simmer, C.: Quasi-Vertical Profiles—A new way to look at polarimetric radar data. J. Atmos. Ocean. Technol., 33, 551–562. doi:10.1175/JTECH-D-15-0020.1, 2016.

Schneebeli, M., and Berne, A.: An Extended Kalman Filter Framework for Polarimetric X-Band Weather Radar Data Processing. J. Atmos. Oceanic Technol., 29, 711–730, https://doi.org/10.1175/JTECH-D-10-05053.1, 2012.

Serrar, S., Delrieu, G., Creutin, J.D., Uijlenhoet, and R.: Mountain Reference Technique: Use of mountain returns to calibrate weather radars operating at attenuating wavelengths. J. Geophys. Res. – Atmospheres, 105(D2): 2281-2290. DOI :10.1029/1999JD901025, 2000.

Sideris, I. V., Gabella, M., Erdin, R., and Germann, U.: Real-time radar–raingauge merging using spatio-temporal co-kriging with external drift in the alpine terrain of Switzerland. Q. J. R. Meteorol. Soc., 140, 1097 – 1111, DOI:10.1002/qj.2188S, 2014.

Testud, J, Le Bouar, E., Obligis, E. and Ali-Mehenni, M.: The Rain Profiling Algorithm Applied to Polarimetric Weather Radar. J. Atmos. Oceanic Technol., 17: 332-356. http://dx.doi.org/10.1175/1520-0426(2000)017%3C0332:TRPAAT%3E2.0.CO;2, 2000.

Thurai, M., and Bringi, V.N.: Drop axis ratios from 2D video disdrometer. J. Atmos. Oceanic Technol., 22, 963–975. https://doi.org/10.1175/JTECH1767.1, 2005.

Trömel, S., Kumjian, M.R., Ryzhkov, A.V., Simmer, C., and Diederich, M.: Backscatter differential phase – estimation and variability. J. Appl. Meteor. Climatol., 52, 2529-2548, doi: 10.1175/JAMC-D-13-0124.1, 2013.

Westrelin, S., Meriaux, P., Tabary, P., and Aubert Y.: Hydrometeorological risks in Mediterranean mountainous areas - RHYTMME Project: Risk Management based on a Radar Network. ERAD 2012 7th European Conference on Radar in Meteorology and Hydrology, June 2012, Toulouse, France. 6 p., hal-01511157, 2012.

Yu, N., Gaussiat, N., and Tabary, P.: Polarimetric X-band weather radars for quantitative precipitation estimation in mountainous regions. Q. J. Royal Meteorol. Soc., 144(717), DOI:10.1002/qj.3366, 2018.

Yu, N. and Gaussiat, N.: A monotonic algorithm for estimation of the specific differential phase. Poster presentation during the 10th European Conference on Radar in Meteorology and Hydrology (ERAD 2018), 1-6 July 2018, Ede-Wageningen, The Netherlands, 2018.

745

Table 1. Characteristics of the XPORT and MOUC radar systems

	MOUC radar	XPORT radar
Longitude (decimal degrees)	5.639237	5.762327
Latitude (decimal degrees)	45.147736	45.194150
Altitude (m asl)	ground: 1901 antenna feedhorn: 1917	ground: 213 antenna feedhorn: 228
Frequency (GHz)	9.420	9.400
Antenna diameter (m)	1.8	1.8
3-dB beamwidth (°)	1.28	1.37
Antenna gain (dB)	42	42
Radome	yes	no
Peak power	30 kW, on each polarisation	50 kW, on each polarisation
Pulse length (µs)	2	1
Radial bin size (m)	240	34.2
Receiver dynamic range (dB)	>90	>90
Minimum detectable signal (dBm)	-114	-112
Volume scanning protocol (PPIs with elevation angles in °)	0 / 0.6 / 1.2 / 2 / 3 / 4 / 8 / 14°	3.5 / 7.5 / 15 / 25 / 45°
Volume scanning period (min)	5	~~6~~7
Measured parameters	$Z_h, Z_v, Z_{dr}, \rho_{hv}, \phi_{dp}$,~~$v_r$~~, v_r	

Table 1. Characteristics of the XPORT and MOUC radar systems

Date	Beginning (UTC)	End (UTC)	Altitude range of the ML (m ASL)	Total rain amont (mm)	Maximum rainrate in 10 min (mmh^{-1})	Maximum MRT PIA (dB)
May 12, 2017	12:00	16:00		9.2	8.4	14.2
July 21, 2017	15:30	19:30		35.2	41.7	30.7
August 8, 2017	08:30	14:30		27.9	8.1	30.1
August 31, 2017	07:00	11:30		19.9	15.5	7.6
May 22, 2018	16:00	23:00		16.9	8.4	10.2
May 27, 2018	14:00	17:00		6.9	9.9	6.0
May 28, 2017	13:00	23:00		9.8	9.0	7.7
July 20, 2018	17:00	22:00		12.1	15.6	19.3
August 9, 2018	07:30	15:00		24.8	8.4	19.2

Table 2. Some characteristics of the nine convective events considered in the study of the $\phi_{dp} - PIA$ relationship in rain. The ML detection was performed with the 25°-elevation angle measurements of the XPORT radar using the ~~procedure~~algorithm described in Khanal et al. (2019). The total rain amount and the maximum rainrate ~~come from~~are recorded at the weather station available at the ~~site of the~~ XPORT radar site at IGE. The maximum PIA is derived from the MRT technique by considering the 7.5° elevation data of the XPORT radar.

						May 12th, 2017				August 9th, 2018			
Target	Mean azimuth (°)	Mean range (km)	Range extent (km)	Number of gates	Size (km²)	Mean reflectivity (dBZ)	Standard deviation (dBZ)	10% quantile (dBZ)	90% quantile (dBZ)	Mean reflectivity (dBZ)	Standard deviation (dBZ)	10% quantile (dBZ)	90% quantile (dBZ)
1	2.9	4.1	0.3	51	0.06	48.39	0.21	48.17	48.73	48.29	0.23	48.03	48.62
2	13.2	4.8	1.1	130	0.18	52.19	0.8	51.55	53.17	52.22	0.66	51.62	53.27
3	17.5	5.7	1.5	163	0.27	51.9	0.29	51.61	52.25	52.42	0.50	51.91	53.14
4	24.0	8.6	2.1	133	0.33	51.98	0.51	51.44	52.80	51.87	0.40	51.41	52.39
5	29.0	14.6	0.6	71	0.30	49.44	0.55	48.91	50.01	50.31	0.59	49.63	51.10
6	89.5	17.1	2.4	160	0.79	53.20	0.38	52.81	53.59	52.78	0.43	52.34	53.53
7	95.3	14.5	1.4	95	0.40	54.12	0.23	53.91	54.30	53.96	0.21	53.72	54.20
8	98.4	13.2	2.1	120	0.45	51.02	0.50	50.59	51.67	52.13	0.39	51.69	52.67
9	101.2	13.1	2.0	156	0.58	48.95	0.23	48.71	49.18	49.50	0.12	49.37	49.66
10	119.7	12.1	2.8	92	0.32	49.36	0.21	49.11	49.59	50.23	0.12	50.07	50.39
11	124.8	11.8	2.3	242	0.82	51.04	0.53	50.50	51.84	52.02	0.32	51.63	52.43
12	130.1	11.9	1.9	240	0.82	51.43	0.90	50.48	52.63	54.63	0.52	54.08	55.30
13	135.1	12.0	1.7	271	0.94	50.20	0.87	49.33	51.48	53.24	0.78	52.34	54.35
14	238.8	11.4	2.2	221	0.73	52.97	0.67	52.20	53.59	52.86	0.58	52.11	53.60
15	243.8	10.7	0.8	187	0.58	52.63	0.59	51.97	53.46	53.79	0.35	53.37	54.23
16	248.8	10.5	0.9	162	0.49	53.62	0.41	53.11	54.02	52.96	0.37	52.53	53.50

~~**Table 3**~~

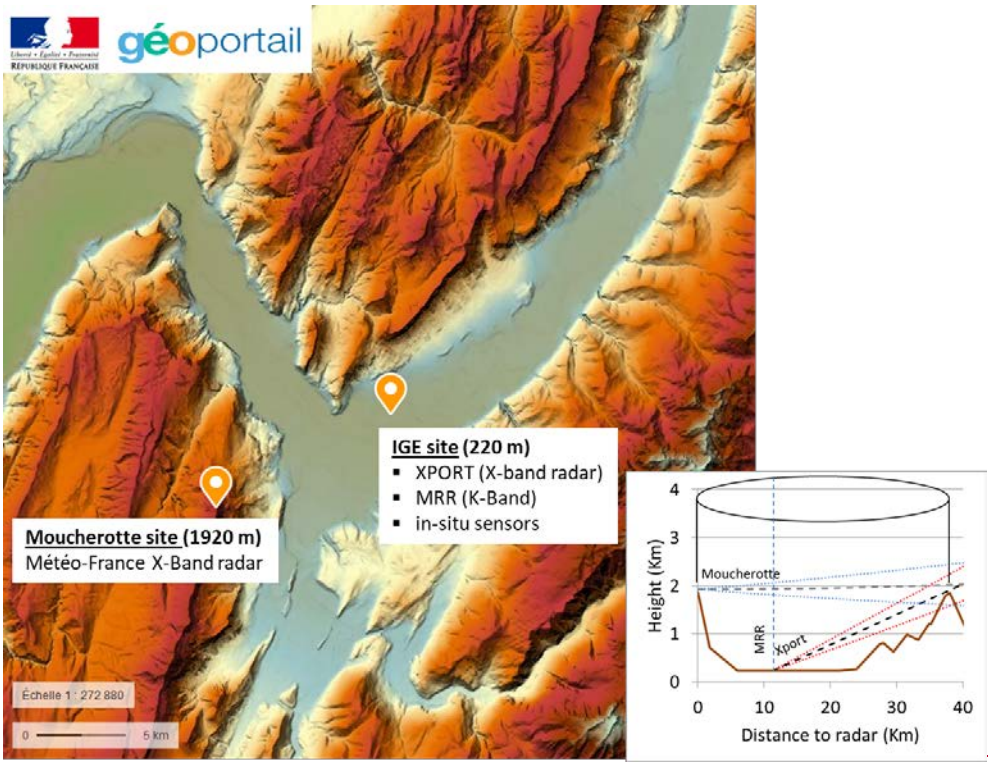

Date	Beginning (UTC)	End (UTC)	Minimum altitude of the ML bottom (m asl)	Total rain amont (mm)	Maximum rainrate in 10 min (mm h^{-1})	Maximum MRT PIA (dB)
May 12, 2017	12:00	16:00	2000	9.2	8.4	14.2
July 21, 2017	15:30	19:30	3000	35.2	42.0	30.7
August 8, 2017	08:30	14:30	3700	27.9	48.0	30.1
August 31, 2017	07:00	11:30	3200	19.9	15.5	7.6
May 22, 2018	16:00	23:00	2000	16.9	8.4	10.2
May 27, 2018	14:00	17:00	2700	6.9	9.9	6.0
May 28, 2017	13:00	23:00	2500	9.8	9.0	7.7
July 20, 2018	17:00	22:00	2700	12.1	15.6	19.3
August 9, 2018	07:30	15:00	3000	24.8	8.4	19.2

805

Table 3: Geometrical characteristics and apparent reflectivity statistics for the 16 mountain targets selected for the XPORT radar at an elevation angle of 7.5°. The mean, standard deviation, 10 and 90% quantiles of the apparent reflectivity time series are given for the first and last convective events in the considered period (see Table 2).

					May 12th, 2017				August 9th, 2018			
Target	Mean azimuth (°)	Mean range (km)	Number of gates	Size (km²)	Mean reflectivity (dBZ)	Standard deviation (dBZ)	10% quantile (dBZ)	90% quantile (dBZ)	Mean reflectivity (dBZ)	Standard deviation (dBZ)	10% quantile (dBZ)	90% quantile (dBZ)
1	2.9	4.1	51	0.06	48.39	0.21	48.17	48.73	48.29	0.23	48.03	48.62
2	13.2	4.8	130	0.18	52.19	0.80	51.55	53.17	52.22	0.66	51.62	53.27
3	17.5	5.7	163	0.27	51.90	0.29	51.61	52.25	52.42	0.50	51.91	53.14
4	24.0	8.6	133	0.33	51.98	0.51	51.44	52.80	51.87	0.40	51.41	52.39
5	29.0	14.6	71	0.30	49.44	0.55	48.91	50.01	50.31	0.59	49.63	51.10
6	89.5	17.1	160	0.79	53.20	0.38	52.81	53.59	52.78	0.43	52.34	53.53
7	95.3	14.5	95	0.40	54.12	0.23	53.91	54.30	53.96	0.21	53.72	54.20
8	98.4	13.2	120	0.45	51.02	0.50	50.59	51.67	52.13	0.39	51.69	52.67
9	101.2	13.1	156	0.58	48.95	0.23	48.71	49.18	49.50	0.12	49.37	49.66
10	119.7	12.1	92	0.32	49.36	0.21	49.11	49.59	50.23	0.12	50.07	50.39
11	124.8	11.8	242	0.82	51.04	0.53	50.50	51.84	52.02	0.32	51.63	52.43
12	130.1	11.9	240	0.82	51.43	0.90	50.48	52.63	54.63	0.52	54.08	55.30
13	135.1	12.0	271	0.94	50.20	0.87	49.33	51.48	53.24	0.78	52.34	54.35
14	238.8	11.4	221	0.73	52.97	0.67	52.20	53.59	52.86	0.58	52.11	53.60
15	243.8	10.7	187	0.58	52.63	0.59	51.97	53.46	53.79	0.35	53.37	54.23
16	248.8	10.5	162	0.49	53.62	0.41	53.11	54.02	52.96	0.37	52.53	53.50

Table 4: Geometrical characteristics and apparent reflectivity statistics for the 13 mountain targets selected for the MOUC radar at an elevation angle of 0°. The mean, standard deviation, 10 and 90% quantiles of the apparent reflectivity time series are computed over the period January 3rd, 19:00 – 23:55 UTC preceding the rising of the ML at the level of the MOUC radar.

					January 3rd-4th, 2018			
Target	Mean azimuth (°)	Mean range (km)	Number of gates	Size (km²)	Mean reflectivity (dBZ)	Standard deviation (dBZ)	10% quantile (dBZ)	90% quantile (dBZ)
1	40.0	29.52	25	1.55	49.97	1.1	48.70	51.26
2	43.7	26.28	13	0.72	49.90	1.28	48.18	51.36
3	78.0	27.12	24	1.36	48.18	1.44	46.77	50.12
4	84.2	23.64	28	1.39	49.56	0.95	48.37	50.90
5	89.5	23.04	82	3.96	49.09	0.62	48.39	49.80
6	96.0	21.36	78	3.49	49.37	0.75	48.32	50.34
7	101.7	19.92	52	2.17	49.31	1.01	47.83	50.37
8	107.2	22.44	33	1.55	51.94	1.11	50.52	53.22
9	117.0	25.32	38	2.02	51.50	1.03	50.17	52.74
10	121.2	23.52	41	2.02	48.65	1.18	47.28	50.18
11	128.5	28.44	43	2.56	49.38	0.98	48.21	50.59
12	132.5	27.00	25	1.41	50.33	1.24	48.71	51.81
13	160.2	44.88	37	3.48	49.91	1.00	48.69	51.11

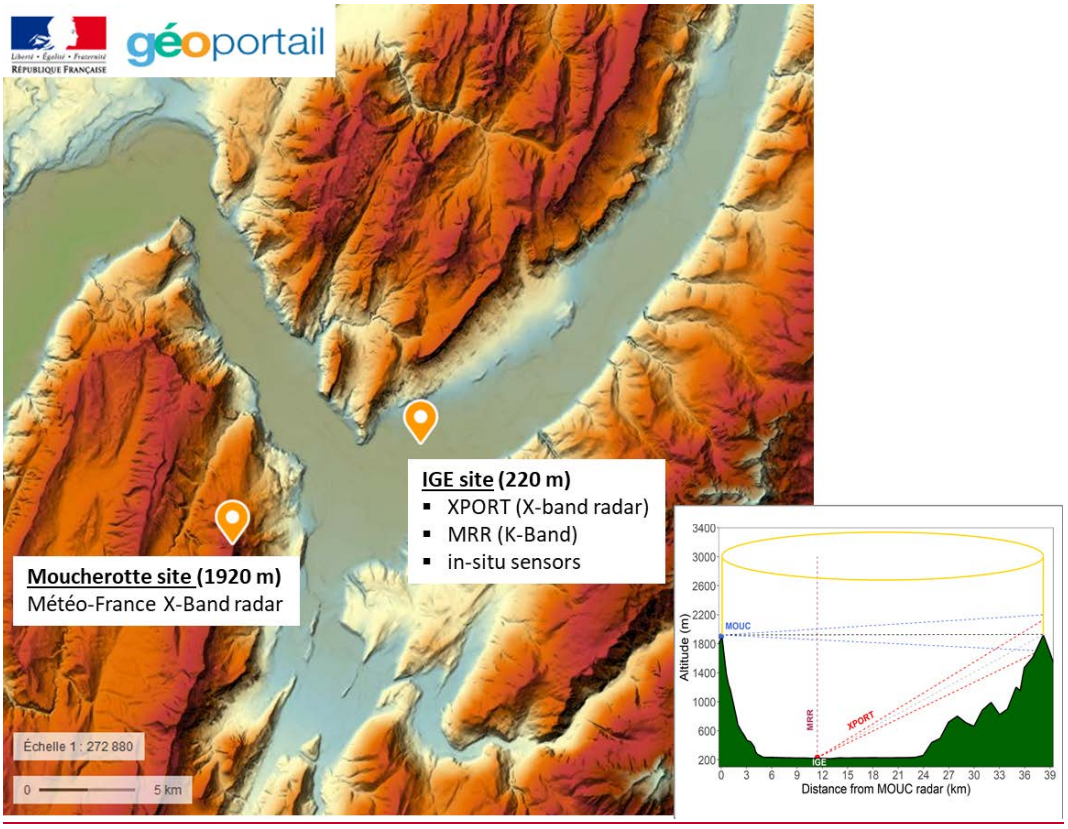

Figure 1. The topographical map of Grenoble is shown along with positions of two radar systems. A vertical cross-section along the line joining the two radar sites is shown in the insert on the bottom right of the figure.

845

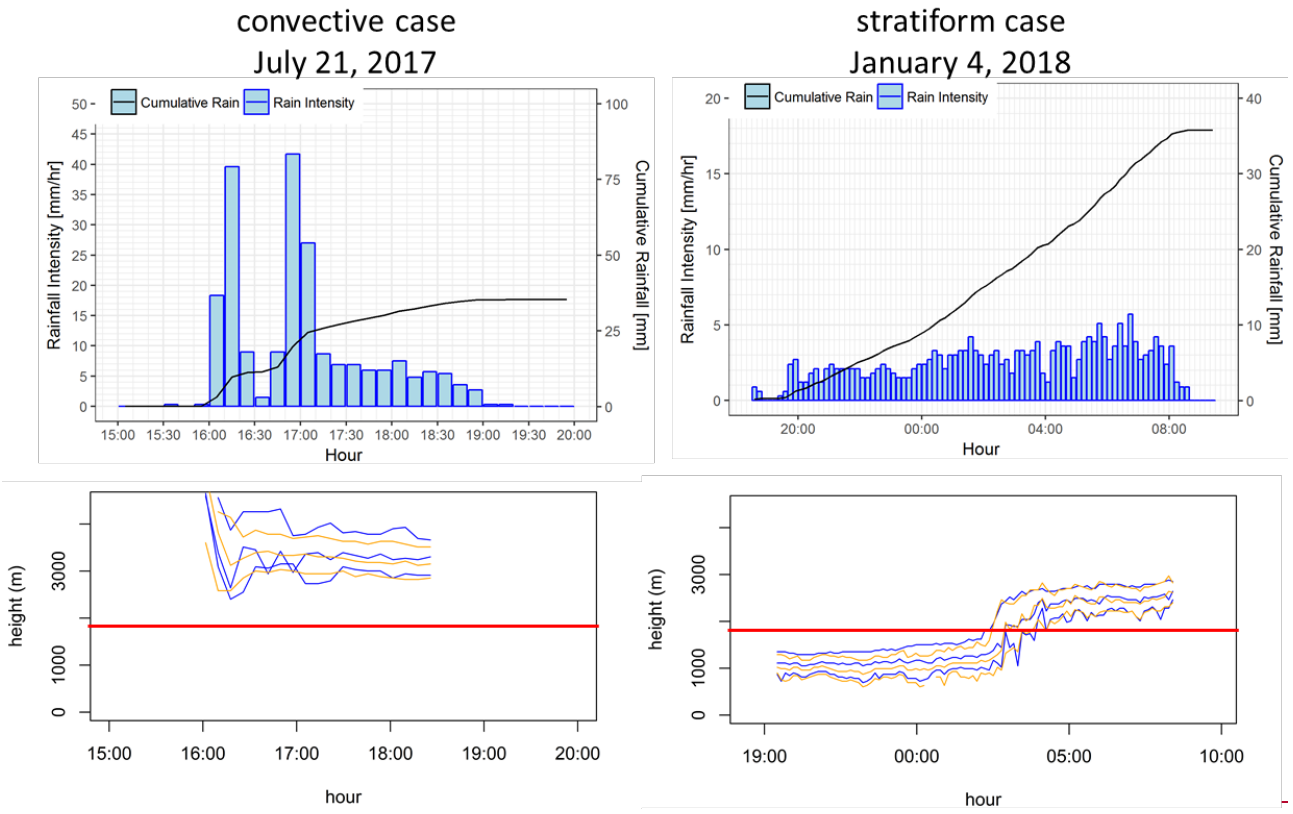
convective case
July 21, 2017
Cumulative Rain
Rain Intensity
Rainfall Intensity [mm/hr]
Cumulative Rainfall [mm]
Hour
stratiform case
January 4, 2018
Cumulative Rain
Rain Intensity
Rainfall Intensity [mm/hr]
Cumulative Rainfall [mm]
Hour
height (m)
hour
height (m)
hour

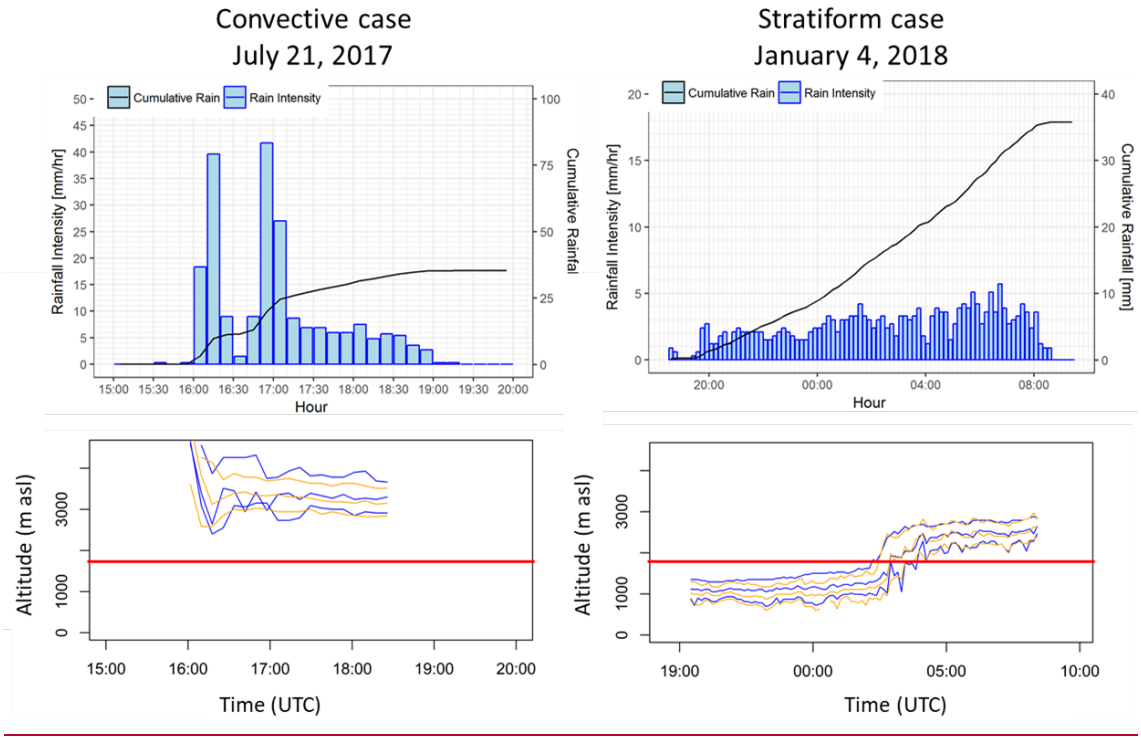

850

Figure 2. Description of ~~the~~ two rain events considered in the present study: left – convective case of July 21, 2017; right – stratiform case of January 4, 2018 ~~; top~~. Top graphs: rainrate and cumulative rainfall timeseries observed at the IGE site ~~-~~; bottom: results of the ML detection algorithm based on XPORT 25°-PPI data. The horizontal red line indicates the altitude of the MOUC radar; see text for details.

855

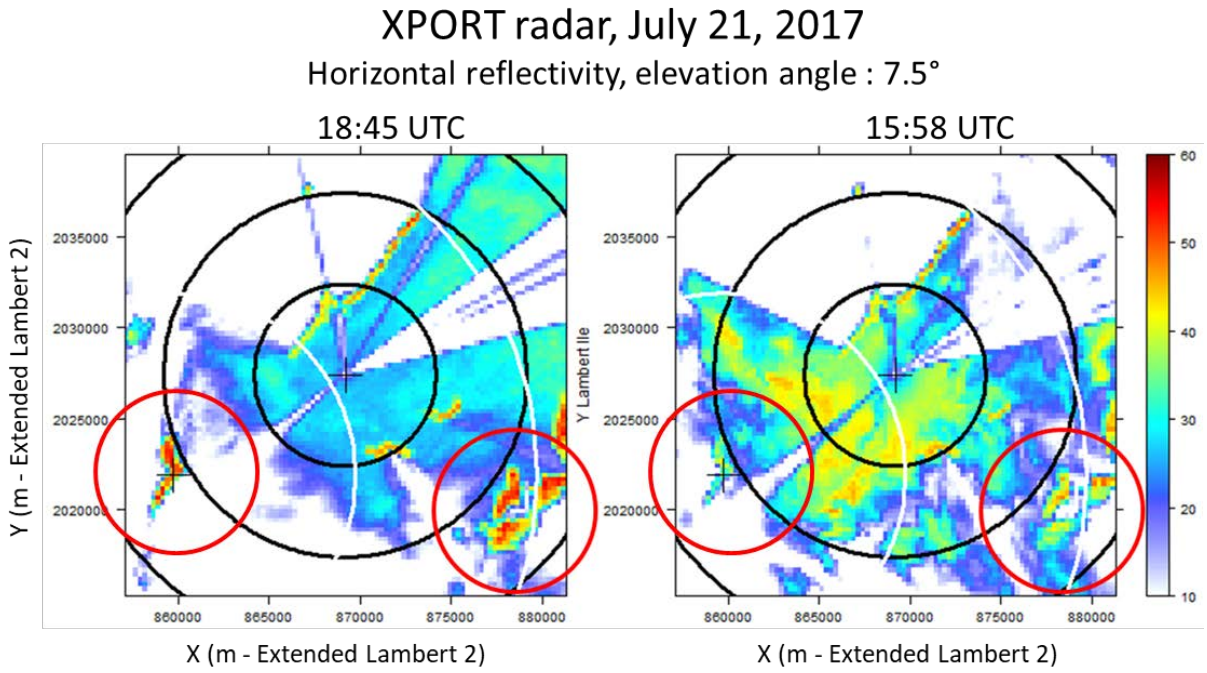

Figure 3. Examples of XPORT 7.5° PPIs of raw reflectivity (~~non~~not-corrected for attenuation) taken for two time steps during the July 21, 2017 convective event. The crosses indicate the location of the two radars and the black / white (5 / 10-km) range markers correspond to the XPORT and the MOUC radar, respectively. The red circles focus the attention of the reader on the mountain returns associated with the Chamrousse (south-east) and the Moucherotte (south-west) ~~mounts~~mountains in between the 10-15 km range.

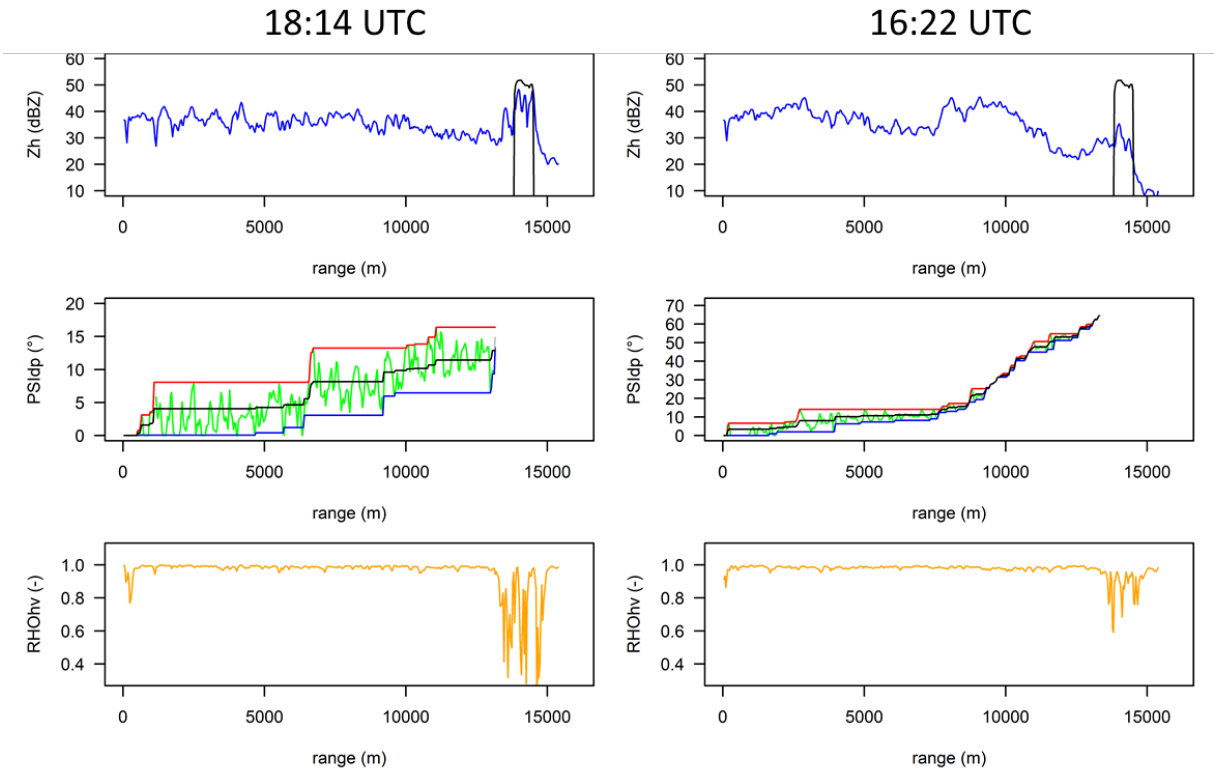
18:14 UTC
16:22 UTC
Zh (dBZ)
PSIdp (°)
RHOhv (-)
range (m)
0
5000
10000
15000

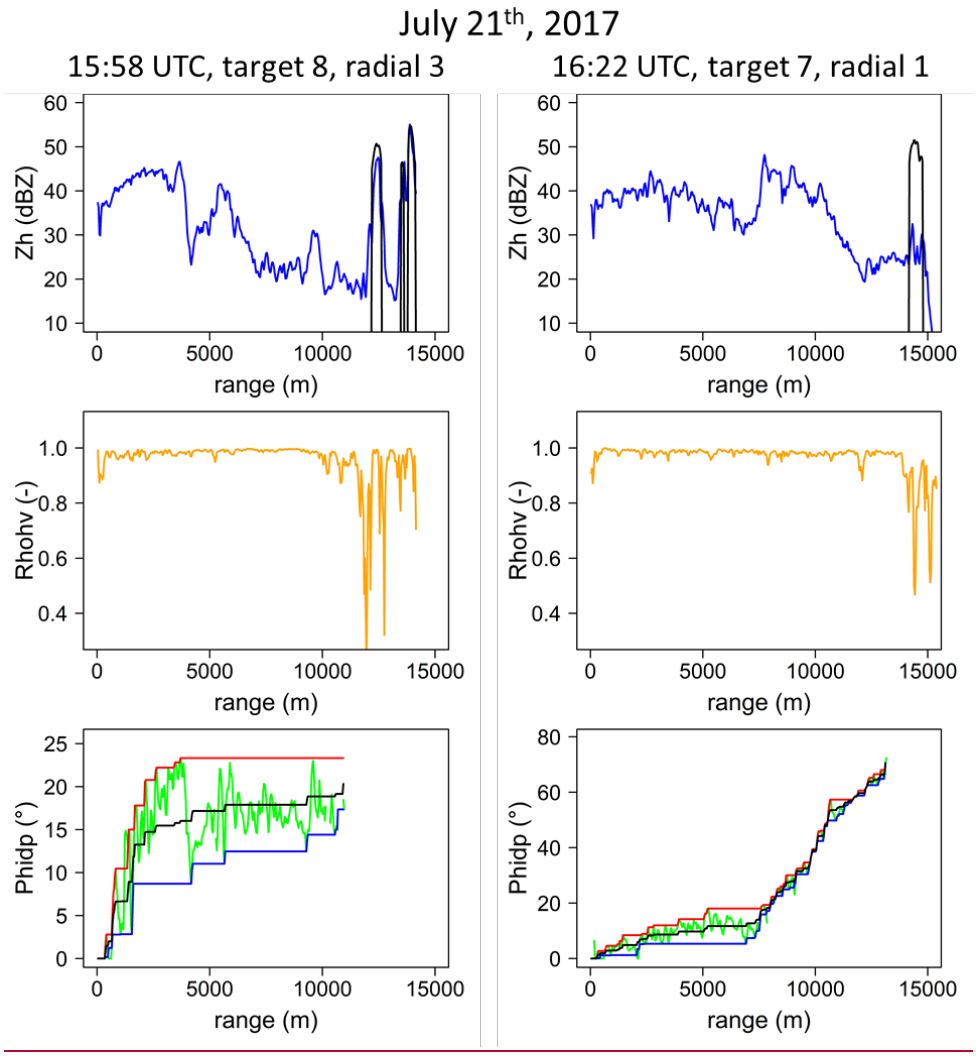

Figure 4. Two examples (left, right) of Z_h, ~~Ψ_{dp}, ρ_{hv}~~ ρ_{hv} and Φ_{dp} range profiles of the XPORT radar (7.5°-PPI) during the July ~~21~~21st, 2017 convective event for one radial of a given mountain target. The raw horizontal reflectivity profiles (top graphs) at the considered time steps (blue) are displayed together with the dry-weather reference target value (black~~) at a range of about 14 km.~~). The ρ_{hv} profiles (middle graphs) are used to detect the rainy gates not affected by clutter at close range and in the region of the mountain target. The bottom graphs display the ~~measured~~raw Ψ_{dp} profiles (green), the upper (red) and lower (blue) envelope curves and the regularized ~~Ψ_{dp}~~Φ_{dp} profiles (black). ~~The ρ_{hv} profiles (bottom graphs) are used,~~

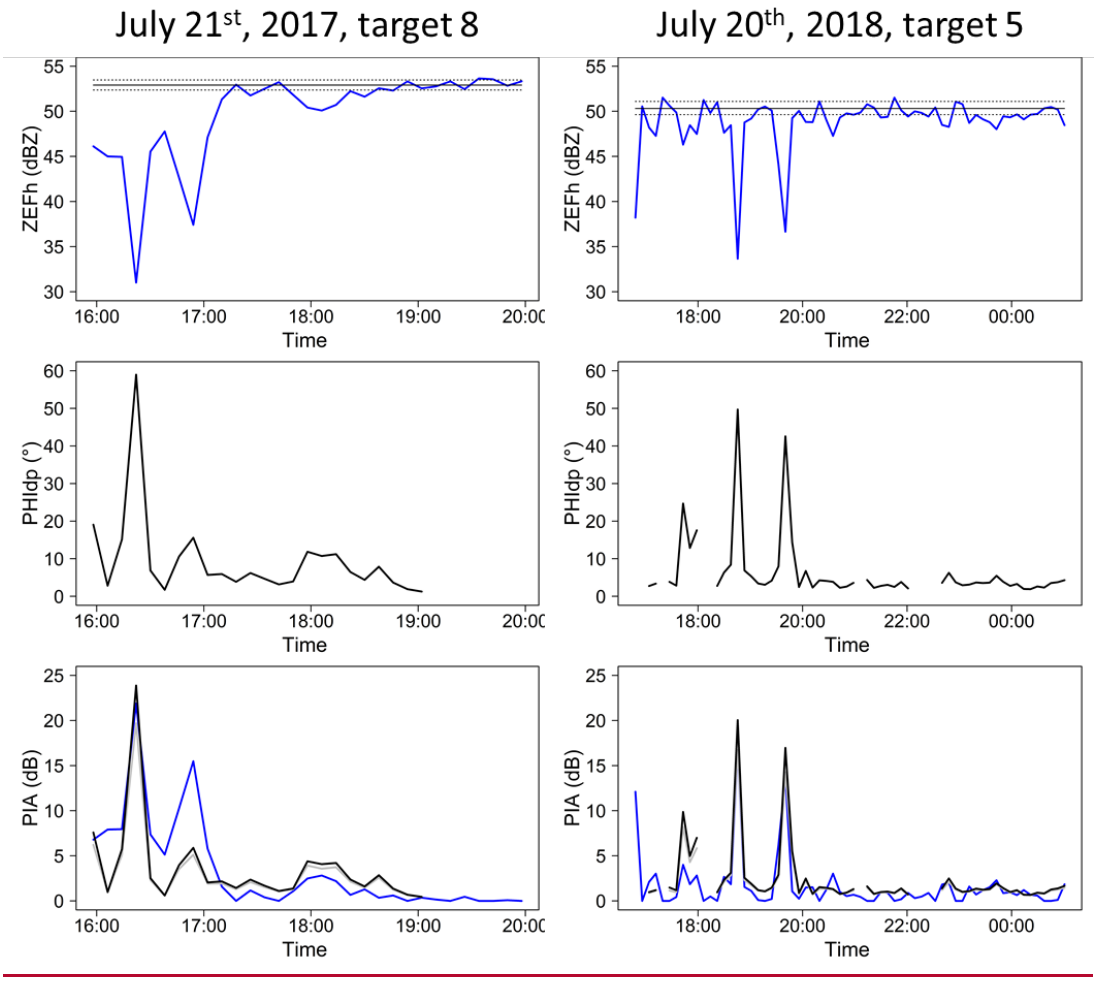

Figure 5. Two examples of time series of the apparent reflectivity of mountain returns for a given target (top graphs), the corresponding Φ_{dp} estimates (middle graphs) and the resulting PIA estimates. The horizontal black lines on top graphs represent the mean (solid line), the 10% and 90% quantiles (dotted lines) of the dry-weather apparent reflectivity of the target. The three lines on bottom graphs correspond to the MRT PIA estimate (blue) and to the polarimetry-derived PIA estimates by using the linear $k - K_{dp}$ relationship (grey) and the non-linear $k - K_{dp}$ relationship (black), derived from DSD measurements at ground level.

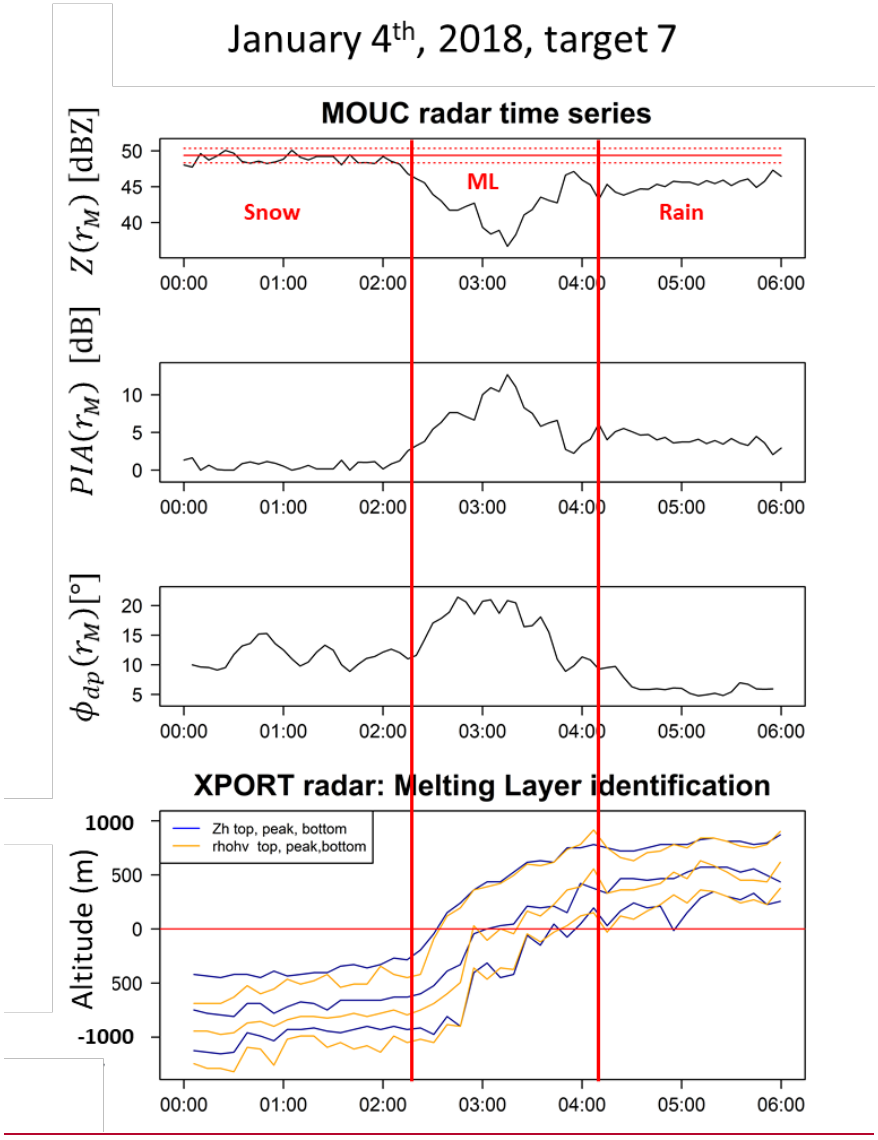

Figure 6. Time series of (i) the apparent reflectivity values of a given mountain reference target together with the dry-weather reference (red horizontal lines for the mean (solid) and the 10% and 90% quantiles (dotted) , (ii) the resulting PIA estimates (dB), (iii) the corresponding $\phi_{dp}(r_M)$ values (°) for the 0°-PPI of the MOUC radar during the January 3-4th, 2018 stratiform rain event. The bottom graph displays the results of the ML detection algorithm performed with the XPORT 25°-PPI data; see text for details.

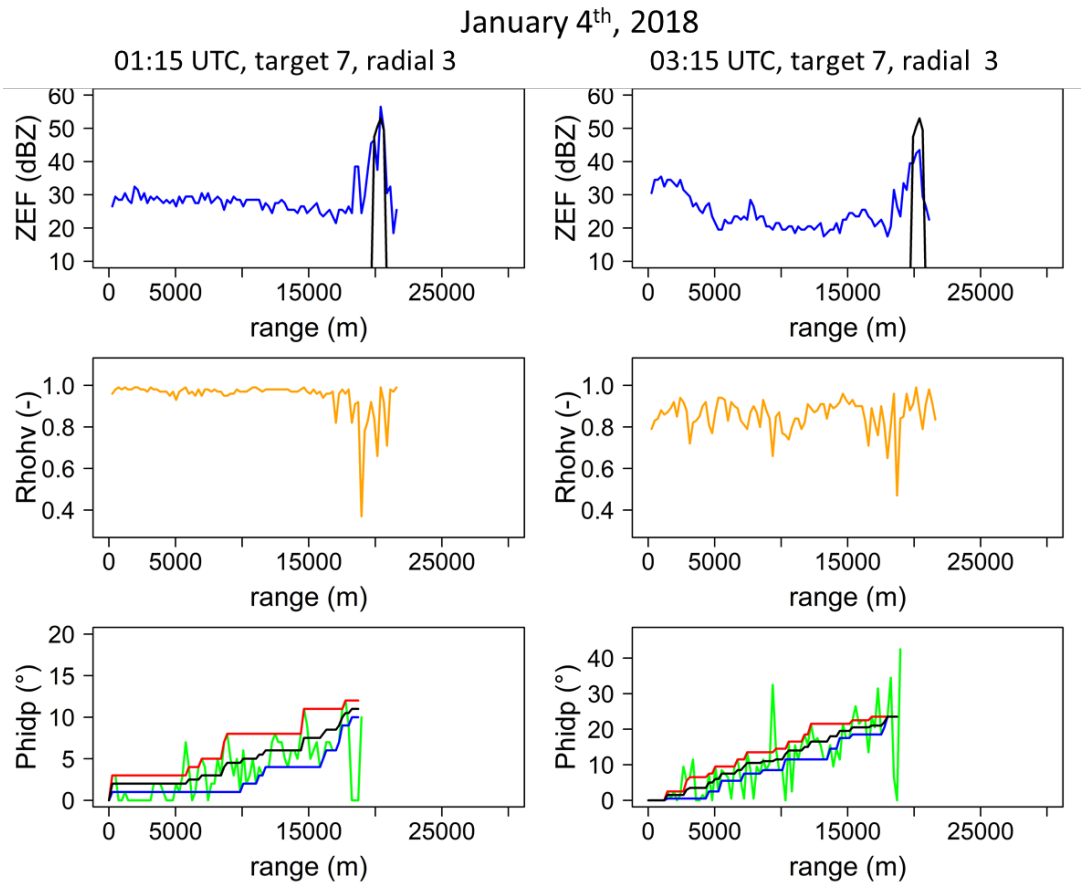

Figure 7. Two examples (left, right) of Z_h, ρ_{hv} and ϕ_{dp} range profiles~~,~~ of the MOUC radar (0°-PPI) during the July 21st, 2017 convective event for one radial of a given mountain target. The raw horizontal reflectivity profiles (top graphs) at the considered time steps (blue) are displayed together with the dry-weather reference target value (black). The ρ_{hv} profiles (middle graphs) are used to detect the rainy gates not affected by clutter at close range and in the region of the mountain target. The bottom graphs display the raw ψ_{dp} profiles (green), the upper (red) and lower (blue) envelope curves and the regularized ϕ_{dp} profiles (black).

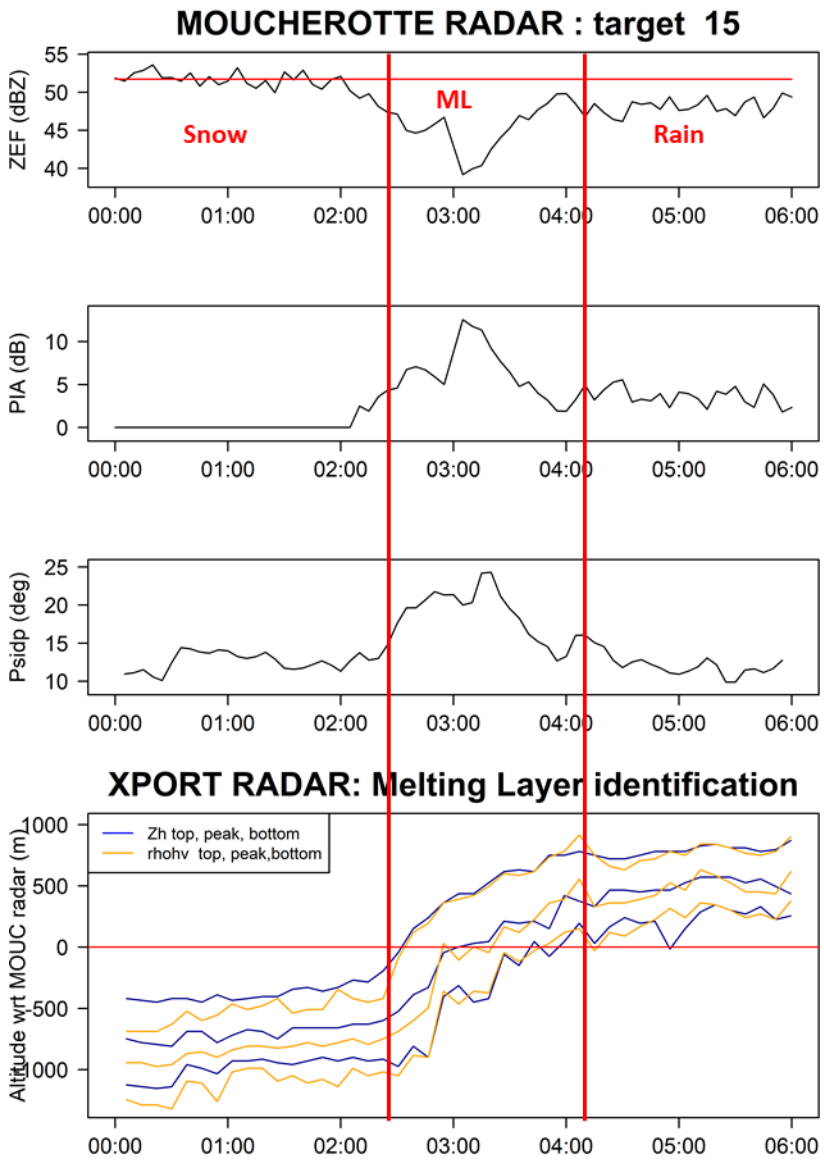

Figure 5. Timeseries of (a) the apparent reflectivity values of a given mountain reference target, (b) the resulting PIA estimates (dB), (c) the corresponding $\psi_{dp}(r_M)$ values (°) for the 0° PPI of the MOUC radar during the January 3-4, 2018 stratiform rain event. The bottom graph (d) displays the results of the ML detection algorithm performed with the XPORT 25° PPI

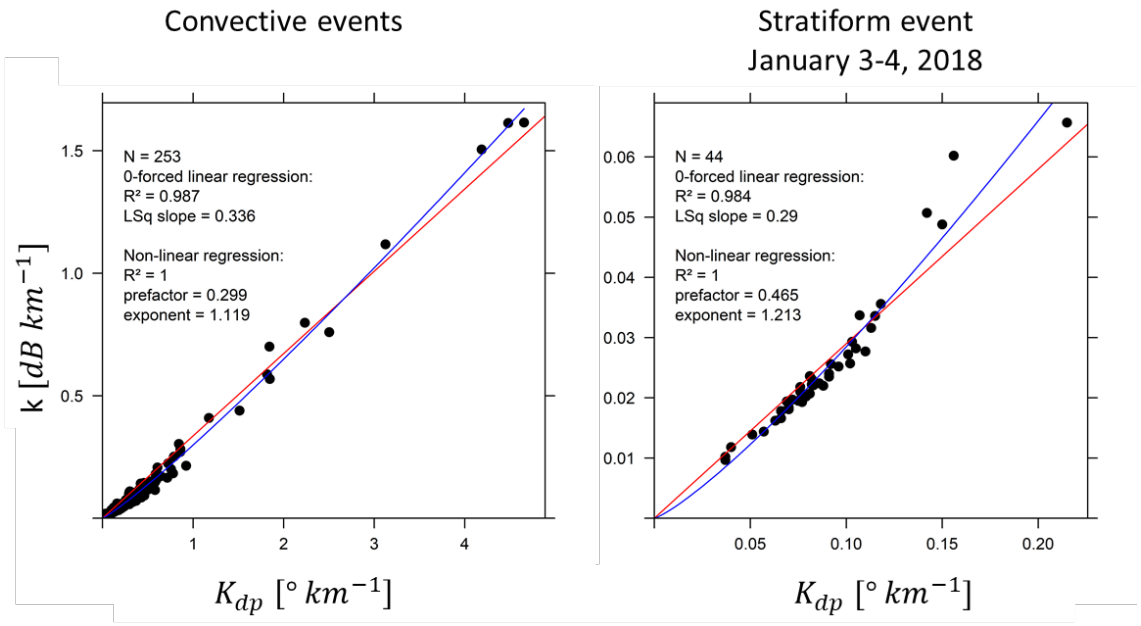

920

~~; see text for details.~~

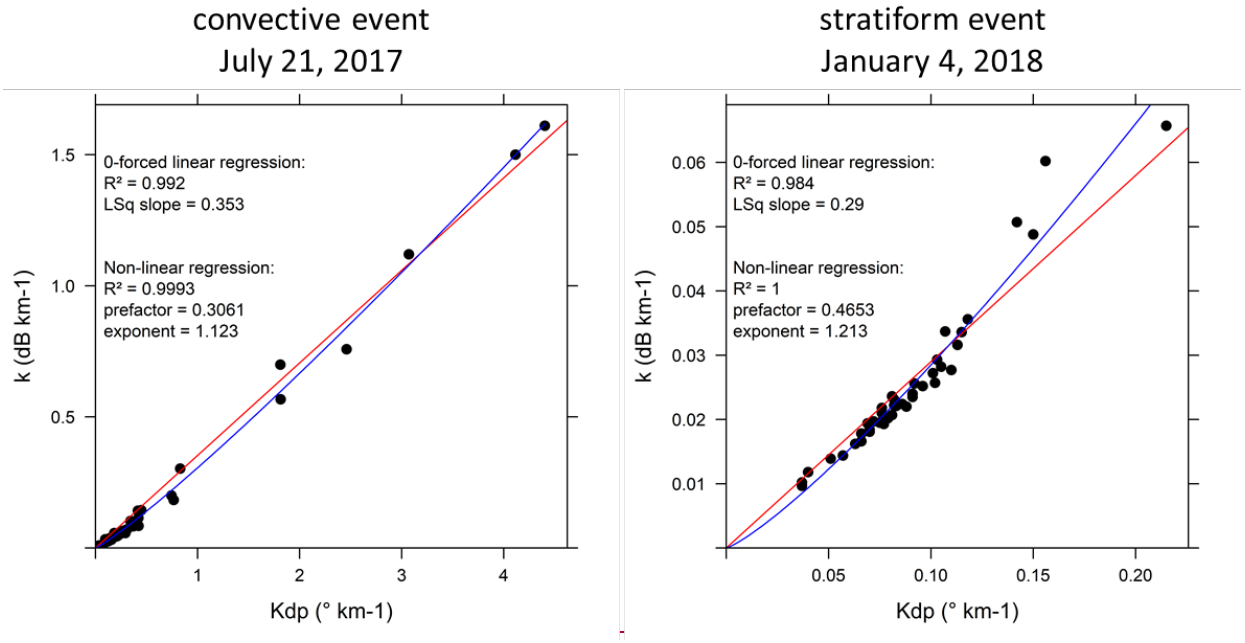

~~Figure 6.~~Figure 8. DSD-derived $k - ~~K_{dp}~~K_{dp}$ relationships for the nine convective ~~event of July 21th, 2017~~events (left) and for the stratiform event of January 3-4th, 2018; see text for details.

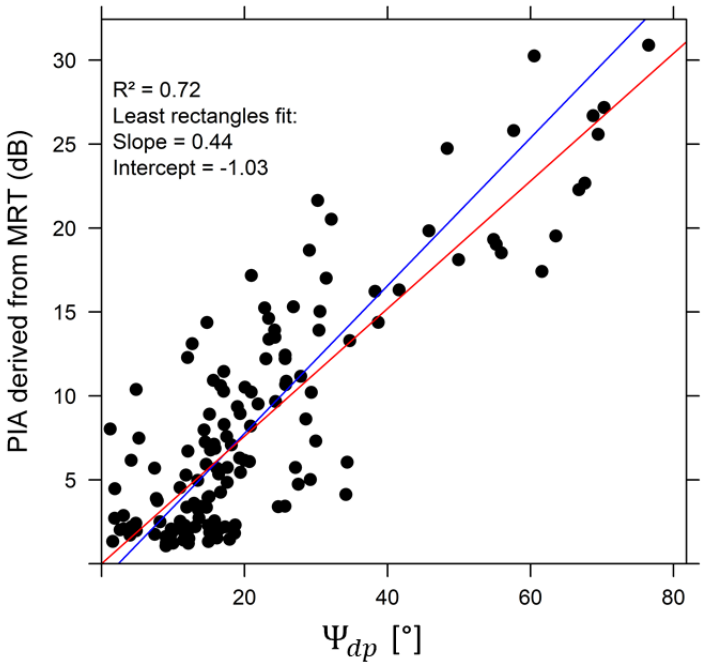

935

~~Figure 7. ψ_{dp} – *PIA* relationship in rain for the convective event of July 21th, 2017.~~

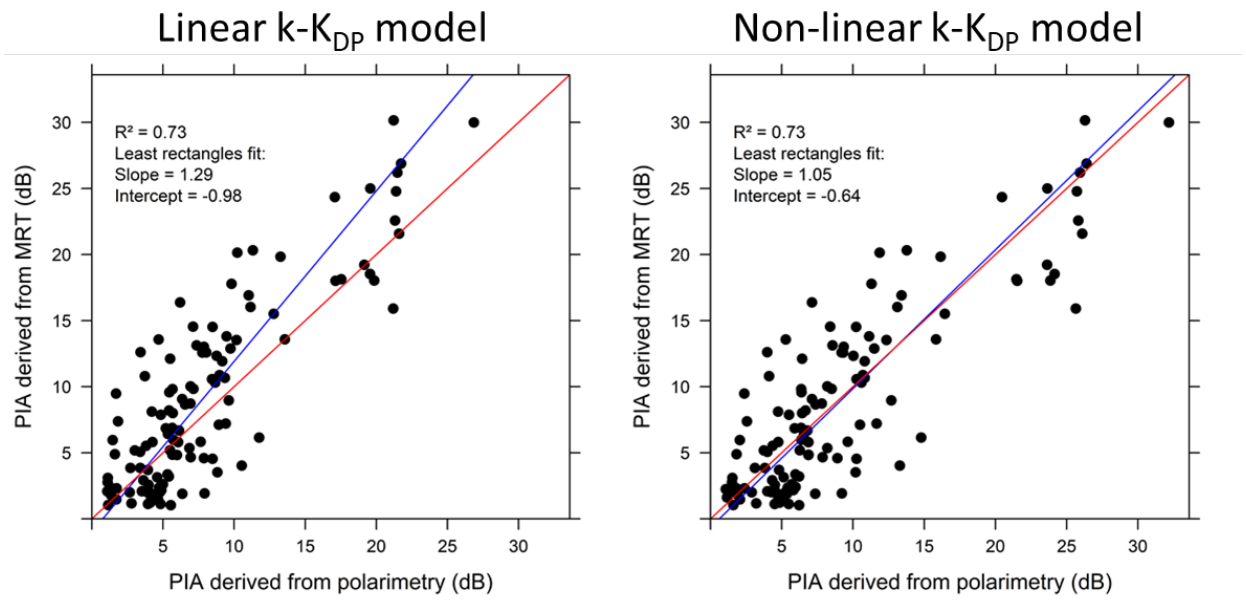
Linear k-K_{DP} model
Non-linear k-K_{DP} model
R^2 = 0.73
Least rectangles fit:
Slope = 1.29
Intercept = -0.98
R^2 = 0.73
Least rectangles fit:
Slope = 1.05
Intercept = -0.64
PIA derived from MRT (dB)
PIA derived from polarimetry (dB)
5
10
15
20
25
30

~~Figure 8.~~

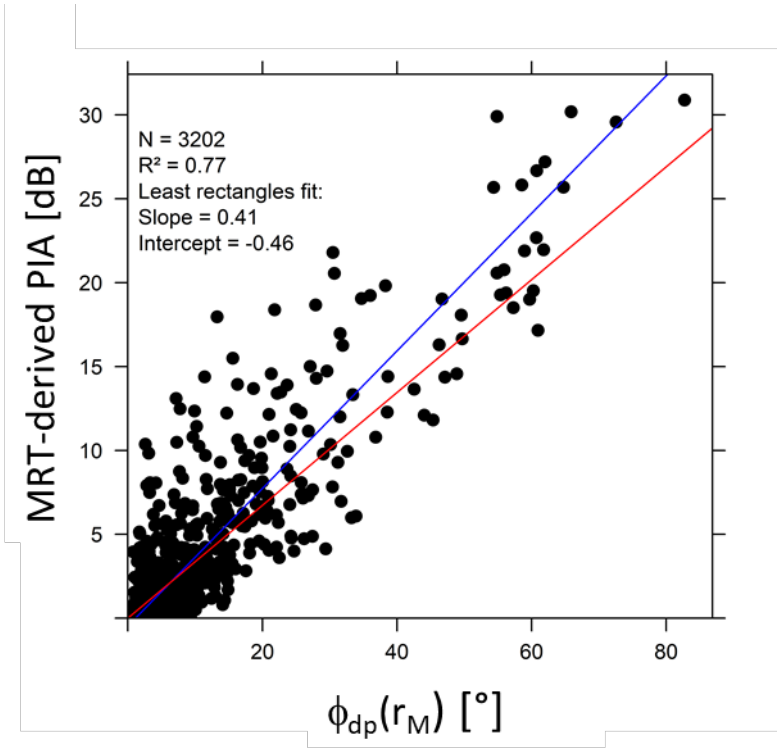

Figure 9. $PIA - \phi_{dp}$ **scatterplot for the nine convective events considered in this study. The blue line corresponds to the least rectangle fit to the data, while the red line corresponds to the linear** $k - K_{dp}$ **relationship derived from the DSD data available at ground level.**

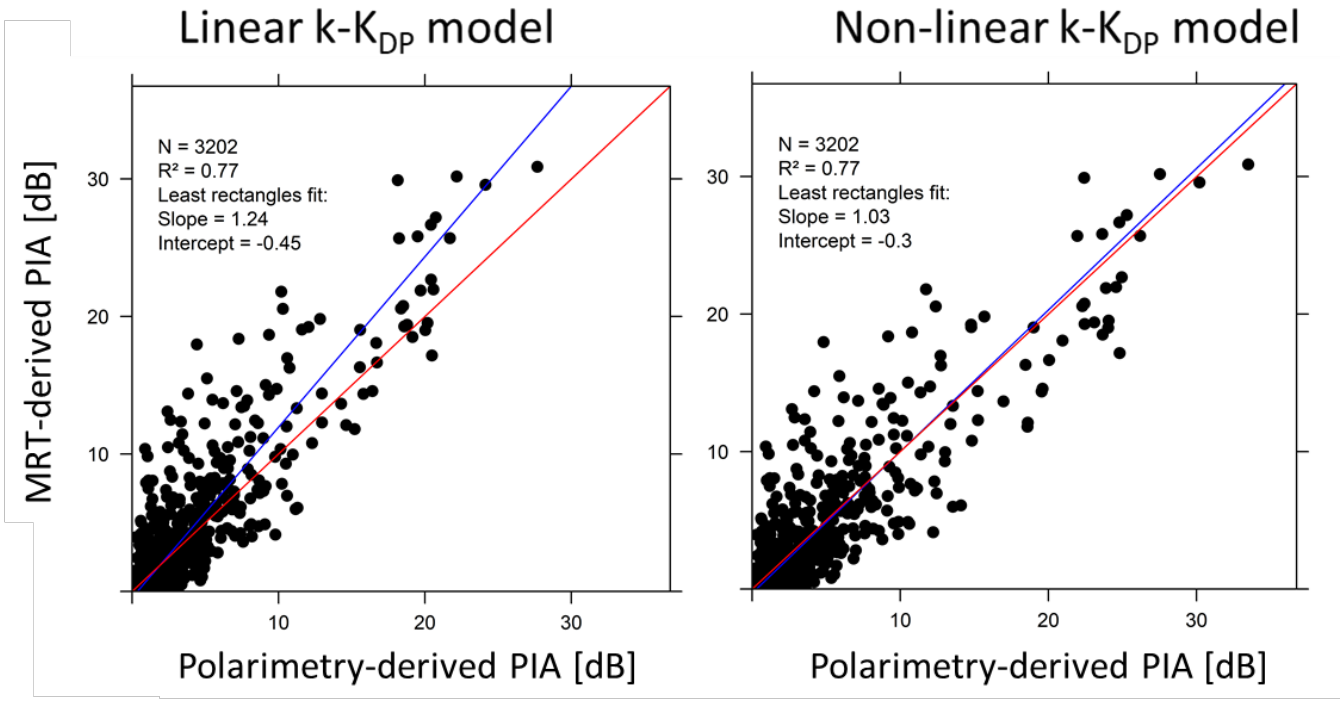

Figure 10. Comparison of the PIAs derived from the Mountain Reference Technique and from polarimetry using the linear k-K_{dp} relationship (left) and the non-linear k-K_{dp} relationship (right) for the nine convective ~~event of July 21th, 2017.~~events. The blue line corresponds to the least-rectangle fit to the data and the red ~~straight~~ line is the 1/1 line.

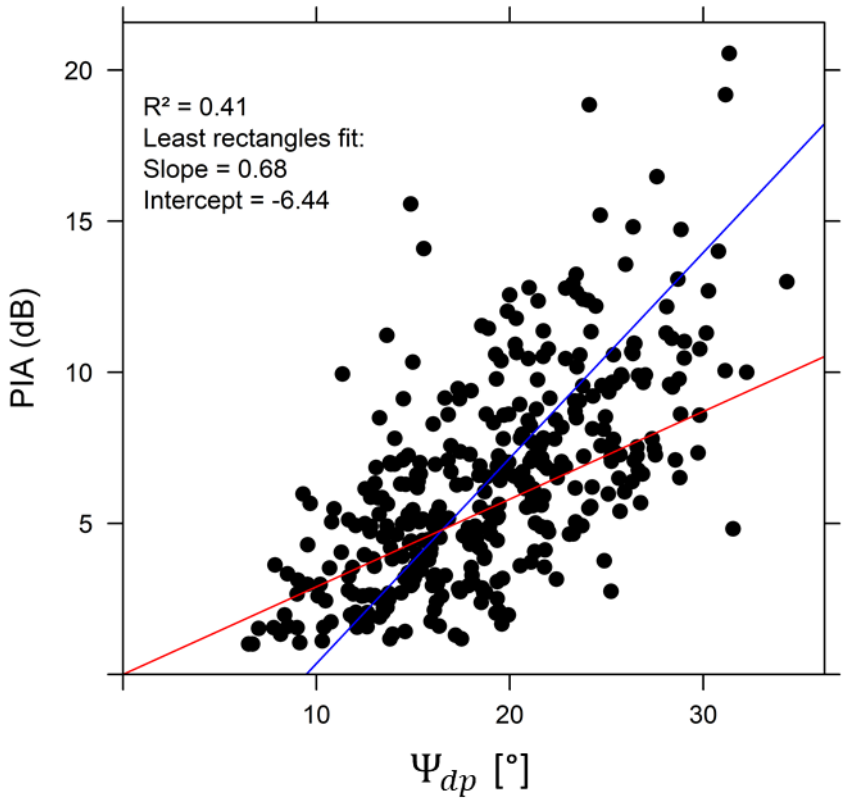
R² = 0.41
Least rectangles fit:
Slope = 0.68
Intercept = -6.44
PIA (dB)
20
15
10
5
10
20
30
Ψ_{dp} [°]

965

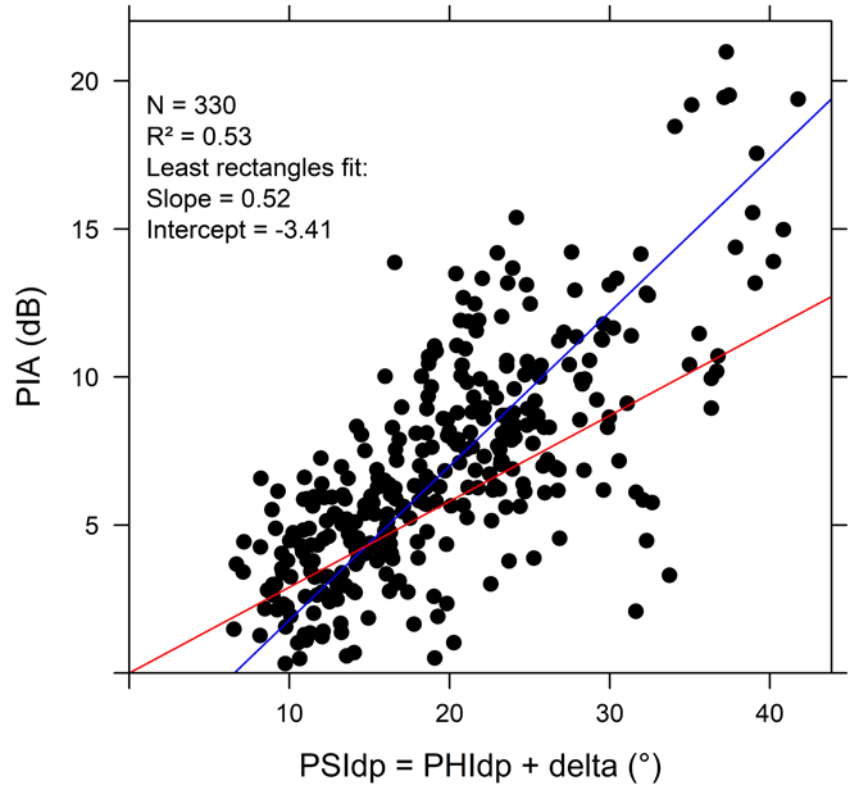

970

Figure ~~9. ψ_{dp} –~~11. *PIA* ~~relationship~~ $-$ ϕ_{dp} scatterplot in the ML for the stratiform event of January 3-4th, 2018. The blue line corresponds to the least rectangle fit to the data, while the red line corresponds to the linear $k - K_{dp}$ relationship derived from the DSD data available at ground level.

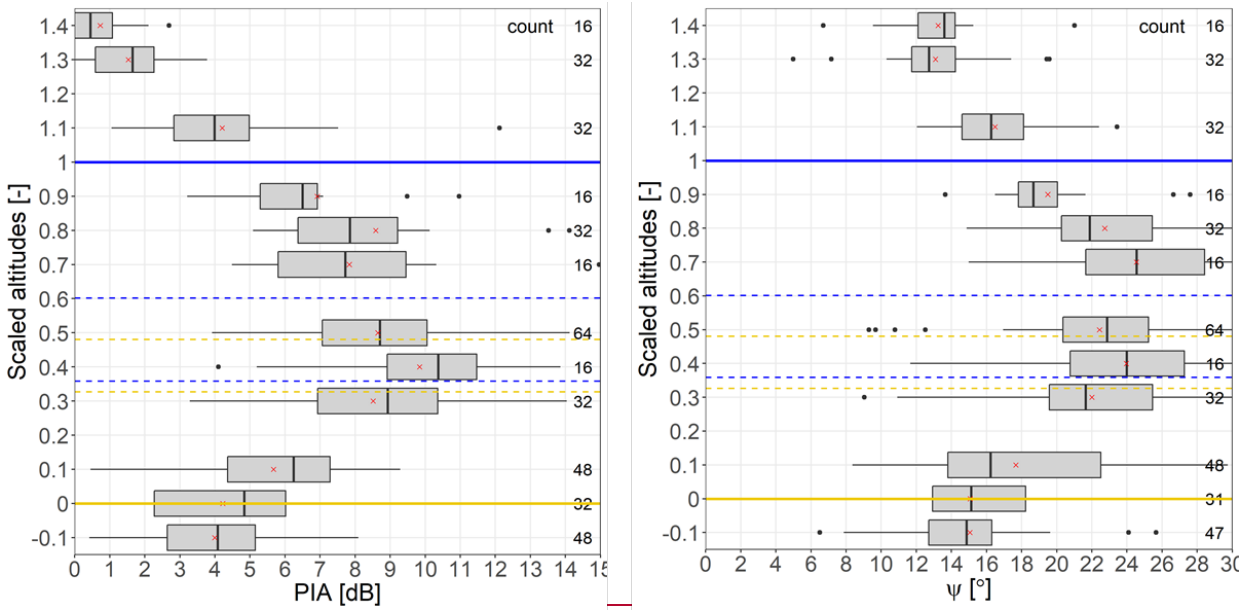
count
16
32
32
16
32
16
64
16
32
48
32
48
Scaled altitudes [-]
PIA [dB]
count
16
32
32
16
32
16
64
16
32
48
31
47
Scaled altitudes [-]
ψ [°]

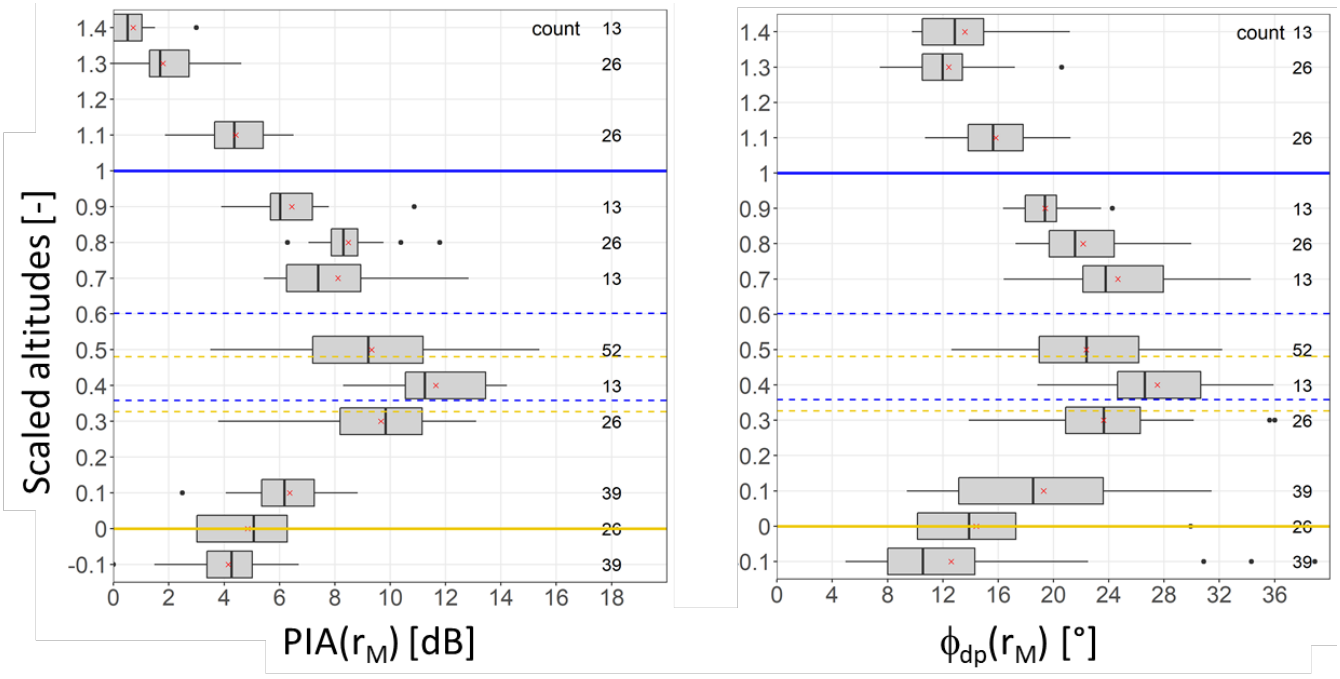

985

Figure ~~10.~~12. Box-plots of the *PIA* and ~~ψ_{dp}~~ϕ_{dp} values within the ML as a function of the scaled altitude (left and right, respectively) for the stratiform event of January 4th, 2018. The horizontal blue and orange continuous lines represent the ML top and bottom, respectively; the dotted horizontal blue and orange lines give the 10 and 90% quantiles of the scaled altitudes of the Zh and ρ_{hv} peak distributions, respectively.

990

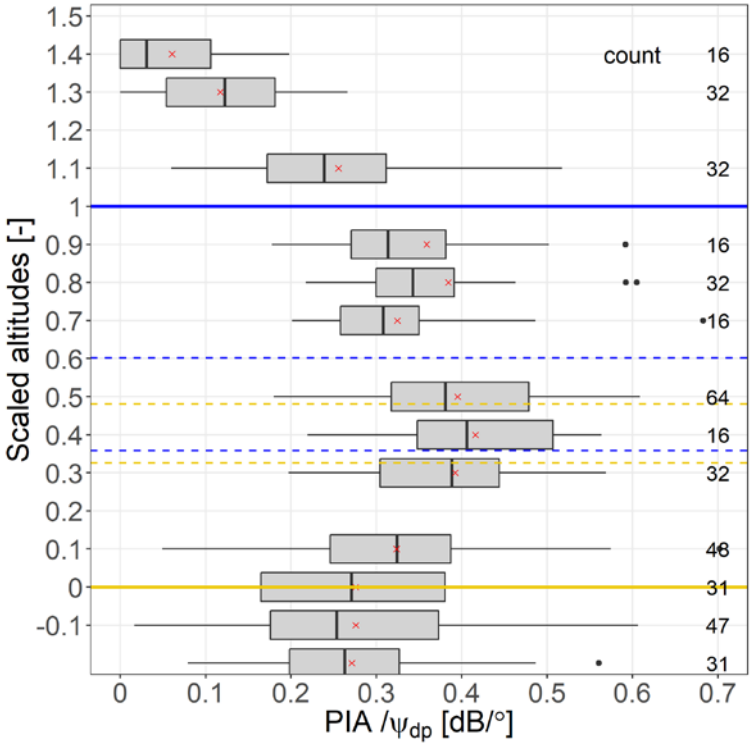
Scaled altitudes [-]
PIA /ψdp [dB/°]
count
16
32
32
16
32
16
64
16
32
46
31
47
31

995

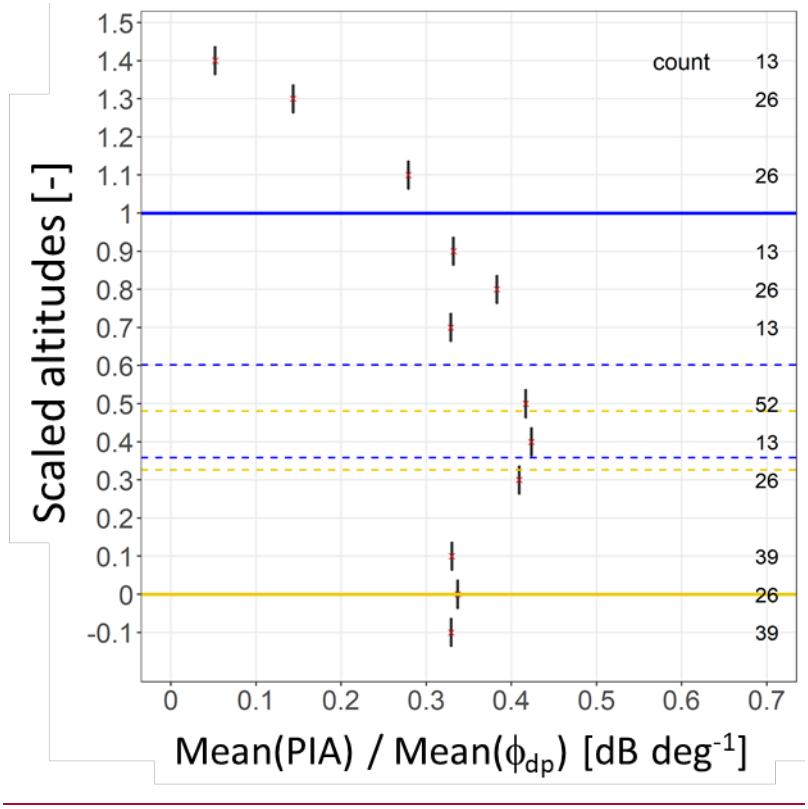

Figure ~~11.~~13. Evolution of the ratio of the mean PIA/ψ_{dp} over the mean ψ_{dp} values within the ML as a function of the scaled altitudes for the stratiform event of January 3-4th, 2018. The horizontal blue and orange lines represent the ML top and bottom, respectively; the dotted horizontal blue and orange lines give the 10 and 90% quantiles of the scaled altitudes of the Zh and ρ_{hv} peak distributions, respectively.